Small-molecule targeting MuRF1 protects against denervation-induced diaphragmatic dysfunction: Underlying molecular mechanisms

Fernando Ribeiro[1], Paulo R. Jannig[2], Siegfried Labeit[3,4], Anselmo S. Moriscot[1*]

[1]Department of Anatomy, Institute of Biomedical Sciences, University of São Paulo, 05508-000 São Paulo, Brazil

[2]Department of Physiology and Pharmacology, Biomedicum, Karolinska Institutet, 171 77 Stockholm, Sweden

[3]Department for Integrative Pathophysiology, DZHK Partner Site Mannheim-Heidelberg, Medical Faculty Mannheim, University of Heidelberg, 68169 Mannheim, Germany

[4]Myomedix GmbH, Neckargemünd, Germany

[*]Correspondent author (e-mail: moriscot@usp.br)

Abstract

Background: Mechanical inactivity rapidly induces diaphragm muscle fibers' contractile dysfunction and atrophy. Diaphragm weakness can impair respiratory function, quality of life, and increase risks of morbidity and mortality. Muscle RING-finger protein-1 (MuRF1) expression is upregulated during denervation and muscle inactivity, and is known to target key muscle proteins for degradation. We previously reported that the small-molecule targeting MuRF1 (MyoMed-205) protects against diaphragm contractile dysfunction and atrophy after 12 hours of unilateral diaphragm denervation (UDD) in rats. In this study, we investigated the mechanisms by which MyoMed-205 protects the diaphragm structure and function during early UDD in rats.

Methods: Male Wistar rats were subjected to unilateral diaphragm denervation (UDD) for 12 hours. Immediately after UDD, rats received either a placebo (vehicle) or small-molecule targeting MuRF1 (MyoMed-205, 50 mg/kg bw), and outcomes were compared with Sham-operated controls. Diaphragm was used for histological, morphometric, transcriptomic (RNA-seq), and protein content (Western Blot) analysis.

Results: UDD induced diaphragm slow- (type I: $p = 0.03$) and fast-twitch (type IIa: $p = 0.04$; type IIb/x: $p = 0.02$) fibers atrophy after 12 hours, which was prevented by MyoMed-205 ($p < 0.05$). Mechanistically, UDD perturbed mechanisms involved with myofiber ultrastructure and contractility, mitochondrial function, proteolysis, and tissue remodeling in the diaphragm. MyoMed-205 enhanced the activation of mechanisms required for sarcomere integrity, calcium handling, antioxidant defense, chaperone-mediated unfolded protein response, and muscle growth. MyoMed-205 also mitigated intramuscular fat deposition and pro-fibrotic responses triggered by UDD.

Conclusion: Small-molecule targeting MuRF1 (MyoMed-205) protects against diaphragm muscle contractile dysfunction and atrophy after 12 hours of UDD. Herein,

we demonstrate that this protective effect involved augmented activation of signaling pathways controlling muscle structure and function, chaperone-mediated unfolded protein, and muscle growth, while mitigating intramuscular fat deposition and pro-fibrotic responses triggered by UDD at the transcriptional and/or protein level.

Keywords: Skeletal muscle; unilateral diaphragm denervation; mechanical unloading; PI3K-Akt-mTOR pathway; ubiquitin-proteasome system; TRIM63; MyoMed-205

Introduction

Breathing is essential for life. This key biological process is regulated by a complex neuromuscular network generating intrathoracic pressures for lung ventilation and gas exchange. The diaphragm functions as the primary inspiratory pump while contributing to other physiological processes (e.g., visceral organization, coughing, and venous hemodynamics). Due to unique evolutionary adaptations and high lifelong contractile activity, the diaphragm might respond distinctly to mechanical inactivity compared to other skeletal muscles [1]. Clinical conditions such as phrenic nerve injury (e.g., thoracic surgery, trauma) and prolonged mechanical ventilation cause profound diaphragm structural and functional changes. Resulting diaphragm muscle weakness and wasting can impair respiratory capacity, exercise tolerance, quality of life, and increase mortality [2].

Understanding how mechanical activity affects diaphragm muscle structure and function has special clinical relevance [for review, see [3,4]. The unilateral diaphragm denervation (UDD) model has been used to investigate the diaphragm adaptations to short- and long-term periods of absent innervation and contractile function. Even short periods (e.g., < 24 hours) of inactivity following UDD significantly decrease diaphragm force-generation capacity [5,6]. Within 24 hours, contractile function loss can accompany slow- and fast-twitch fibers atrophy [6,7], though other findings suggest that fiber size may be less affected initially, especially in slow-twitch fibers [5]. Adaptive responses triggered by UDD include diaphragm ultrastructural changes, myofibrillar protein loss, altered protein balance, increased activation of proteolytic pathways, apoptosis, and muscle tissue remodeling [6,8–13].

Since its discovery in the early 2000s, Muscle RING-finger protein 1 (MuRF1) has been recognized as a key regulator of skeletal muscle mass and function [14,15]. This muscle-specific E3-ligase targets protein clusters controlling muscle contraction, Ca2+ handling, energy metabolism, immune response, and protein breakdown [16–18]. Increased MuRF1 expression/activity occurs in several stress states (e.g., immobilization, denervation, corticosteroids, heart failure, cancer cachexia, aging) and is associated with muscle wasting and weakness, while MuRF1 deletion improves muscle mass and function [19]. Recent advances in small-molecule MuRF1 inhibitors have shown therapeutic potential across multiple conditions, attenuating muscle wasting in heart failure [22–24], cancer cachexia [25], corticosteroid-induced myopathies [22], and diabetes [26]. Notably, MuRF1 deletion or inhibitor protects against early diaphragmatic dysfunction in mechanically ventilated rodents [20,21], and our group previously demonstrated that small-molecule MuRF1 targeting (MyoMed-205) prevents early diaphragm contractile dysfunction and atrophy in rats subjected to UDD [6], suggesting MuRF1 as a promising therapeutic target for counteracting denervation-induced diaphragm muscle weakness and wasting.

This study aimed to investigate the cellular and molecular mechanisms underlying the small-molecule targeting (MyoMed205) mediated protection against diaphragm dysfunction and atrophy in rats subjected to 12 hours of UDD. We hypothesized that 1) MuRF1 plays a key role in denervation-induced diaphragmatic dysfunction and atrophy, and 2) MyoMed-205 differentially regulates signaling pathways controlling diaphragm muscle contractile function, mass, and tissue remodeling during denervation stress.

Material and Methods

Animals

Wistar rats (Male, 2-3 months old) were used in this study. The animals were kept in standard cages under controlled environmental conditions (24 ± 1°C, 12 h/12 h light-dark cycle) with access to standard food and water *ad libitum*. This study was approved and followed the institutional guidelines for animal care and use for research (CEUA ICB USP #8728030320 and #5143091020).

Experimental design

Twenty-four rats were randomly allocated into three experimental groups (*n* = 8): Sham 12h (Sham); UDD 12 hours + vehicle (DNV + VEH); and UDD 12 hours + MyoMed-205 (DNV + 205). After 12 hours, the animals were euthanized under anesthesia, and the denervated right diaphragm muscle (costal portion) was harvested, quickly snap-frozen in 2-methylbutane chilled in liquid nitrogen, and stored at -80°C until further analysis. Diaphragm samples used in this study originate from our previous work [6] (for further details, see supplementary information).

MyoMed-205 formulation and delivery

A detailed description of MuRF1 inhibitor (MyoMed-205, Myomedix GmbH, Germany) formulation for the *in vivo* study is provided in the supplementary information. Briefly, the compound was freshly dissolved in an 8 mL vehicle solution (DMSO-PEG400-Saline 0.9%). The delivery of either vehicle (VEH) or MyoMed-205 (205) treatments was managed in four split doses (2 mL/dose) administered every 3 h interval over the 12-hour experimental period via the caudal vein. Treatments started immediately

following the confirmation of unilateral diaphragm paralysis (for further details, see supplementary information).

Unilateral diaphragm denervation (UDD)

Animals were initially sedated and anesthetized via intraperitoneal administration of acepromazine (2.5 mg/kg bw), followed after 30 minutes by the administration of ketamine (100 mg/kg bw) and xylazine (5 mg/kg bw). After reaching the surgical plane, the right phrenic nerve was exposed and transected at the rat's lower neck region. The absence of right diaphragm dome contractile activity was used to confirm the denervation's efficacy. Then, the surgical wound was sutured and managed with antiseptics. During the post-operative period, animals were allowed to recover from anesthesia in individual cages with *ad libitum* access to food chow and water. (for further details, see supplementary information).

Diaphragm muscle fiber typing and size analysis

Cryosections (8 µm thick) from the right costal diaphragm muscle were prepared using a cryostat at −20°C (Leica CM1850, Germany). Muscle fiber typing (MyHC I, IIA, IIB/X) was performed via immunofluorescence assay (see antibodies in Table S1). Photomicrographs were acquired using Axio Scope A1 microscope (Zeiss, Germany). Diaphragm fibers' type distribution and cross-sectional area (CSA) were assessed with ImageJ (Fiji, NIH, USA). Representative muscle fiber type distribution and CSA values were determined as the average from 300 measurements per sample of previously unanalyzed muscle fibers (for further details, see supplementary information).

Oil Red O (ORO) Staining

Diaphragm muscle cryosections were stained with ORO to assess the intramuscular lipid content. Photomicrographs were acquired using Axio Scope A1 microscope (Zeiss, Germany). Representative number of positive ORO (ORO+) muscle cells and intracellular lipid content were determined based on measurements of 300 fibers per sample (for further details, see supplementary information).

Transcriptomic profiling (RNA-seq)

Total RNA was extracted from the diaphragm using TRIzol (Life Technologies, Carlsbad, CA). RNA integrity was analyzed using Bioanalyzer 2100 (Agilent, Santa Clara, CA, USA) (Table S2). Four samples of each experimental group with the highest purity and integrity levels were selected for global gene expression analysis (Figure S1). Approximately ~1 ug of sample total RNA was used for cDNA library preparation performed according to the Illumina mRNA stranded poly-A tail enrichment Kit manufacturer's instructions (Illumina, San Diego, CA). RNA sequencing was carried out using the Illumina NextSeq 2000 (NextSeq 2x100pb, 20 million paired-end reads depth). These procedures were performed by NGS Soluções Genômicas (Piracicaba, Brazil).

For bioinformatic analysis, quality control of raw reads was performed using the FastQC toolkit (Babraham Bioinformatics). The reads were then aligned to the mRatBN7.2 rat genome using STAR. Feature count was performed using featureCounts, and differential expression analyses were generated in R using the DESeq2 package with adaptive log-fold change shrinkage estimator from the ashr package Pathway analysis was carried out by Gene Set Enrichment Analysis (GSEA) using a pre-ranked list of genes by log2Fold-Change and Molecular Signatures

Database, and hallmark pathways gene sets for pathway analysis. Transcriptome-related raw files and data can be found in the Gene Expression Omnibus (GEO) repository (GSE305304) (for further details, see supplementary information).

Western Blotting

Diaphragm samples were powdered in a liquid nitrogen-chilled mortar and homogenized in RIPA buffer containing protease and phosphatase inhibitors (ThermoFisher #78445). Homogenates were centrifuged and the collected and stored at −80°C until further analysis. Protein concentration was determined by the Bradford method with bovine serum albumin (BSA) as the standard. Protein was loaded onto polyacrylamide gel (SDS-PAGE), separated via electrophoresis (100V), and transferred to polyvinylidene difluoride (PVDF) membrane (Thermo Fisher Scientific, #88518, Rockford, IL, USA) using wet-transfer system (100 V, 350 mA, for 120 min). Ponceau red staining was used to assess protein transfer efficacy. Membranes were incubated with primary and secondary antibodies (Table S1). Membranes were incubated with ECL substrate (Immobilon Forte, Millipore #WBLUF0500) for 5 minutes before signal detection using C-digit blot scanner (Li-Cor, USA) for chemiluminescent detection, or with BCIP/NBT substrate (Sigma #B1911) for colorimetric detection. Alpha-tubulin was used as a loading control for data normalization, and densitometry analysis was performed using ImageStudio software (for further details, see supplementary information).

Statistical Analysis

Data analysis was performed Excel, Prism and R. For the analysis of the transcriptomic data, refer to the respective section above and supplementary

information. For the analysis of histological, morphometric, and protein expression levels, the Shapiro-Wilk test was used to assess data normality. One-way ANOVA followed by Tukey's post-hoc test, or the Kruskal-Wallis followed by Dunn's test, were used for multiple comparisons between groups, for parametric and non-parametric data, respectively. Data are presented as mean ± standard deviation and statistical significance was accepted as $p < 0.05$.

Results

Transcriptomic profiling reveals mechanisms underlying MyoMed-205-mediated protection against denervation-induced diaphragmatic dysfunction and atrophy

To investigate how denervation might impair diaphragm muscle structure and contractile function, as reported previously [6], we performed a global gene expression analysis of the rat's diaphragm following 12 hours of UDD. Additionally, we compared the transcriptomes of MyoMed-205-treated animals with untreated animals to investigate the mechanisms underlying the MyoMed-205-mediated protective effects. For this purpose, animals were treated either with vehicle (DNV_VEH) or MyoMed-205 (DNV_205), and results were compared with Sham controls (Figure 1A).

Principal component analysis (PCA) demonstrated significant transcriptomic alterations in DNV_VEH compared with Sham. On the other hand, MyoMed-205 caused no evident changes in the clustering pattern compared with DNV_VEH (Figure 1B). DESeq2 analysis was performed to identify differentially expressed genes (DEGs) for each condition (Padj < 0.05). We detected 1563 DEGs in DNV_VEH (873 upregulated, 690 downregulated) and 3487 DEGs in DNV_205 (1935 upregulated, 1552 downregulated), compared with Sham. We found 69 DEGs particularly

responsive to MyoMed-205 treatment compared with DNV_VEH (Figure 1B), of which 7 were upregulated and 62 downregulated (see Table 1). Hierarchical clustering analysis revealed five gene clusters regulated by UDD and MyoMed-205 (Figure 1C).

Gene Set Enrichment Analysis (GSEA) was subsequently employed to identify biological pathways modulated by UDD and MyoMed-205, including hallmark pathways (Figure 1D), molecular functions (Figure 1E), and cellular compartments (Figure 1F). UDD significantly altered the expression of genes associated with muscle contraction, mitochondrial structure/function, inflammatory responses, proteolysis, apoptosis, and muscle tissue remodeling, compared with Sham. Interestingly, MyoMed-205 upregulated pathways involved with antioxidant response, chaperone-mediated unfolded protein response, ribosome biogenesis, protein synthesis, and cell growth. Conversely, MyoMed-205 downregulated genes associated with adipogenesis and extracellular matrix collagen deposition compared with DNV_VEH and Sham groups (Figure 1D-F).

Effects of MyoMed-205 upon mechanisms that control skeletal muscle structure and contractile function

We previously reported that 12 hours of UDD promotes muscle fibers contractile dysfunction and atrophy [6]. Herein, our histomorphometric analysis confirmed a significant decrease in diaphragm fiber size across all types (Sham vs. DNV_VEH vs. DNV_205, mean ± SD - Type I: 1537 ± 269 vs. 1184 ± 91 vs. 1588 ± 342; Type IIa: 1750 ± 295 vs. 1307 ± 139 vs. 1795 ± 497; Type IIb/x: 3601 ± 788 vs. 2449 ± 308 vs. 3741 ± 1153 μm^2, $p < 0.05$, $n = 8$) following 12 h of UDD (type I: $p = 0.03$; type IIa: $p = 0.04$; and type IIb/x: $p = 0.02$) compared with Sham. UDD caused comparable

atrophy levels among the fiber types, despite a trend indicating a noticeable effect in fast-twitch type IIb/x fibers compared with slow-twitch type I fibers ($p = 0.06$). Fiber type relative distribution remained unchanged (Figure 2A-B). MyoMed-205 significantly protected against UDD-associated fiber atrophy ($p < 0.05$, $n = 8$), without showing fiber type-specific effect or affecting relative distribution (Figure 2A-B).

To gain mechanistic insights into the protective effects of MyoMed-205, we examined the expression levels of genes and proteins involved in the control of muscle structure and contraction. Significant changes in genes regulating synaptic vesicle membrane and muscle fiber structure/function were observed following 12 h of UDD (Figure 2C). Noteworthy, MyoMed-205 selectively enhanced the expression of genes involved with sarcomere organization and integrity, Z-disk structure, mechanotransduction, and intercellular communication (e.g., Tcap, Actn1, Pdlim3, Cryab, Ankrd1, Zyx, Sdc4, Sorbs1, Tpm4, Bag3 and Gja1) (Figure 2C-D).

Furthermore, UDD affected calcium handling pathways as indicated by downregulation of key calcium handling genes (e.g., RyR1, SERCA1, and SERCA2) (Figure 2E) and increased phospholamban protein levels compared with Sham (Figure 2F). MyoMed-205 enhanced S100A1 gene expression, a calcium-binding protein that positively regulates the activity of calcium channels, concomitantly with suppression of denervation-induced phospholamban protein expression (Figure 2E-F).

UDD negatively affects the transcription of genes associated with mitochondrial dysfunction and oxidative stress, while MyoMed-205 enhances the transcription of antioxidant factors

Mitochondrial structure and function are essential for the maintenance of skeletal muscle function and homeostasis. Therefore, we assessed mitochondrial alterations following 12 h of UDD and MyoMed-205 in the diaphragm. Following 12 hours of UDD, significant changes were observed in the transcription of genes that control mitochondrial structure and function. Key mitochondrial biogenesis regulators (e.g., Ppargc1a) and dynamics mediators (e.g., Opa1, Mfn1, Mfn2) were markedly downregulated (Figure 3A). Genes encoding mitochondrial structural complexes (Figure 3B-C), as well as those regulating energy metabolism via oxidative phosphorylation and fatty acid oxidation (Figure 3D), were also markedly downregulated, further suggesting rapid changes in the expression of genes that regulate mitochondrial dynamics and function. Moreover, we observed increased transcriptional activation of the reactive oxygen species (ROS) pathway (Figure 3E). Interestingly, MyoMed-205 upregulated the expression of a subset of genes involved with the redox balance and antioxidant response (e.g., Nrf1, Nfe2l2, Sirt1, Sod2, Prdx1, Prdx6, and Gclc) (Figure 3E).

MyoMed-205 enhances activation of pathways regulating ribosome biogenesis, protein synthesis, and cell growth under UDD-induced stress

Denervation can negatively affect muscle mass by altering protein synthesis rate and promoting negative protein net balance. We evaluated the impacts of UDD and the MyoMed-205 upon pathways involved with cell growth, proliferation, and survival. Noteworthy, Myc target genes (Figure 4A), the KRAS (Figure S3), and mTORC1 signaling pathways were found upregulated after 12 hours of UDD (Figure 4B). Strikingly, MyoMed-205 enhanced RNA processing and transcription (Figure S2), further amplifying these effects by increasing the expression of genes associated with

the PI3K-Akt-mTOR pathway (Figure 4B), ribosome biogenesis, translation initiation (Figure 4C), and androgen response (Figure S3). Consistent with gene expression changes, MyoMed-205 increased PI3K-Akt-mTOR pathway activation at the protein level (Figure 4D).

UDD upregulates proteolytic signaling pathways, while MyoMed-205 improves chaperone-mediated unfolded protein response at the transcriptional level

Denervation can also activate proteolytic pathways contributing to muscle wasting. Thus, we evaluated the effect of UDD and MyoMed-205 upon pathways associated with muscle protein breakdown and programmed cell death. UDD significantly upregulated distinct proteolytic and stress response pathways, including immune and inflammatory responses (Figure S4), the IL6-JAK-STAT3 pathway (Figure 5A), unfolded protein response (Figure 5B), ubiquitin-proteasome pathway (Figure 5C-D), p53 pathway (Figure 5E), and apoptosis (Figure 5F) at the transcriptional level. Remarkably, MyoMed-205 enhanced the expression of genes mediating chaperone-mediated unfolded protein response (Figure 5B). Noteworthy, we noticed a relatively higher gene expression of E3-ligases linked to muscle wasting, including Fbxo32 (i.e., Atrogin-1, log2fold = 0.96 vs 0.20, values relative to Sham; padj = 0.59) and TRIM63 (i.e., MuRF1, log2fold = 2.27 vs 1.44, values relative to Sham; padj = 0.59) in MyoMed-205 treated animals compared with vehicle, despite not reaching statistical significance (Figure 5C). In line with this, protein levels of these E3-ligases and K48-ubiquitinated proteins were not significantly changed, except for MuRF2, a close relative of MuRF1, which was upregulated by UDD but prevented by MyoMed-205 (Figure 5D).

MyoMed-205 mitigates denervation-induced expression of genes involved with intramuscular lipid accumulation and ECM-collagen deposition

Prolonged inactivity can lead to sustained muscle cell stress and damage, triggering apoptosis and tissue remodeling responses such as intramuscular fat deposition and fibrosis. Therefore, we evaluated how UDD and MyoMed-205 affect these responses in the diaphragm after 12 hours.

Following UDD, we observed a significant upregulation in adipogenic-related gene expression compared with Sham (Figure 6A), although no changes were detected in adipogenic or lipid droplet-related proteins within this period (Figure 6B). Oil Red O (ORO) staining revealed significantly increased ORO-positive (ORO+) cells and intracellular lipid content across distinct fiber phenotypes (i.e., predominantly oxidative fibers <2500 μm², and predominantly glycolytic fibers >2500 μm²). Interestingly, MyoMed-205 downregulated adipogenesis at the transcriptional level (Figure 6A), attenuating intramuscular lipid accumulation triggered by UDD (Figure 6C).

Moreover, UDD upregulated the expression of genes associated with the TGF-β signaling (Figure S5), collagen trimmer (Figure 7A), basement membrane (Figure 7B), and extracellular-matrix collagen deposition (Figure 7C), compared with Sham. On the other hand, MyoMed-205 downregulated the pro-fibrotic response at the transcriptional level (Figure 7A-C).

Discussion

Lack of contractile activity can rapidly induce diaphragm muscle weakness and wasting, contributing to impaired respiratory function, morbidity, and mortality. This

clinical condition is particularly found in patients undergoing phrenic nerve injury or prolonged mechanical ventilation during intensive care unit (ICU) treatment. Therefore, understanding the mechanisms underlying UDD and how to prevent them by identifying potential novel therapeutic targets is an important, and yet unmet, clinical need. We recently reported that small-molecule targeting MuRF1 (MyoMed-205) protects against early diaphragm muscle fiber contractile dysfunction and atrophy in rats undergoing 12 hours of UDD [6]. In the present study, we identified molecular mechanisms that are linked to the MyoMed-205-mediated protection against this loss in fibers' contractile force and size. Briefly, MyoMed-205 upregulated pathways associated with: 1) muscle fiber structure and contractile function; 2) antioxidant defense; 3) chaperone-mediated unfolded protein response; 4) muscle cell growth, while downregulated pathways involved with 5) intramuscular lipid accumulation and 6) ECM collagen deposition at the transcriptional and/or protein level.

Disrupted calcium homeostasis has been reported in response diaphragm mechanical inactivity, as evidenced by downregulation of key genes like SERCA1, impaired RyR1 activity, decreased Ca2+ sensitivity, and sarcoplasmic reticulum (SR) calcium leakage [27]. Consistent with these findings, we observed a rapid downregulation of key genes involved in calcium handling, alongside increased phospholamban protein levels, a negative regulator of SERCA activity. MuRF1 has been reported to directly target proteins involved in calcium handling and muscle contraction [16–18]. Interestingly, MyoMed-205 prevented denervation-induced elevation of phospholamban protein levels, while upregulating S100A1 gene expression, although its protein levels remained unchanged. S100A1 is a calcium-binding protein that enhances RyR1 and SERCA activity and thus improves excitation-contraction coupling in striated muscles

[28]. S100A1 overexpression has been shown to rescue cardiac function throughout enhanced Ca^{2+} handling and myofibrillar protein Ca^{2+} responsiveness in heart failure models [29]. These findings suggest that MyoMed-205 may partially preserve calcium handling homeostasis via upregulation of S100A1 and blockade of phospholamban, likely contributing to preserving diaphragm contractile function, as we previously reported [6].

Myofibrillar protein loss and post-translational modifications (PTMs) induced by prolonged inactivity can also impair diaphragm force-generation capacity. ROS-induced oxidative modifications of muscle proteins have been detected as early as 12 hours of UDD. Our data revealed rapid downregulation of key genes for mitochondrial function and augmented activation of oxidative stress pathways, consistent with our previous findings [6]. MuRF1 can directly regulate certain mitochondrial proteins [16–18]. Here, MyoMed-205 increased the mRNA levels of key antioxidant transcription factors (e.g., Nrf1, Nfe2l2) and enzymes (e.g., Sod2, Prdx1, Prdx6, and Gclc). These findings suggest that MyoMed-205 may improve antioxidant defense mechanisms, which likely contribute to protecting diaphragm muscle fiber structure and function under denervation stress.

Stress-induced unfolded protein response (UPR) activation contributes to maintaining muscle homeostasis under various stress states. Elevated oxidative stress and proteolysis contribute to myofibrillar protein damage, loss, and muscle wasting [30]. Ultrastructural changes, including impaired sarcomere and Z-disk structures, were observed in the diaphragm following denervation [8]. Accordingly, we observed increased UPR pathway activation, which indicates a cellular response against

myofibrillar protein damage and loss after 12 hours of UDD. Interestingly, MyoMed-205 significantly enhanced UPR pathway activation at the transcriptional level by upregulating transcription factors (e.g., XBP1, ATF4) that regulate co-chaperone (e.g., Bag3) and chaperone complexes (e.g., Cryab, Hspa5, Hspa8, Hspb8, Hsp90b1, Dnjb11, Cct5, etc.). MyoMed-205 also upregulated the expression of genes involved in sarcomere integrity maintenance. Bag3 is known to facilitate chaperone-assisted selective autophagy (CASA) process for myofibrillar protein maintenance, and its downregulation impairs contractile function and protein turnover [31]. Bag3 can also interact with alpha B-crystallin (i.e., Cryab) to regulate I-band and Z-disk integrity, while its regulation of Hsp70 chaperone activity protects against damaged protein aggregates and muscle homeostasis [32]. Similarly, chaperone co-inducer BGP-15 attenuates ventilation-induced diaphragmatic dysfunction by activating Hsp72 and reducing myosin post-translational modifications [33]. These findings indicate that MyoMed-205-mediated protective effects might involve enhanced transcriptional activation of chaperones and UPR during UDD stress.

Muscle mass regulation crucially depends on the balance between protein synthesis and degradation. After 12 h of UDD, we observed comparable levels of atrophy across slow- and fast-twitch fibers, despite a trend toward a slightly greater atrophy in type IIb/x fibers was noticed, consistent with previous findings in similar durations (i.e., 24 hours) of diaphragm paralysis [7]. Importantly, some studies also reported no changes in slow- or fast-twitch fiber size at 24 hours of UDD [5]. On the other hand, fiber-type-specific responses seem more pronounced in long-term UDD. Rodents subjected to several days (e.g., 3 – 14) of UDD exhibit predominant atrophy of fast-twitch fibers, particularly of type IIb/x, whereas slow-twitch fibers, which are essential for basal

respiratory function, appear less affected, unaltered, or display transient hypertrophy [5,8,9,12,34]. Yet, the long-term effects of UDD on diaphragm muscle fibers are intricate and remain not completely understood. Clinical observations illustrate this complexity as, in humans, prolonged UDD has been shown to induce progressive diaphragm fiber atrophy, with slow-twitch fibers appearing to be more rapidly and severely affected than fast-twitch fibers [35].

The decline in diaphragm fiber size after 12 hours of UDD indicates a rapid shift towards a predominantly catabolic state. Yet, we simultaneously observed an increased expression of genes linked to protein synthesis and muscle growth (e.g., Myc, MAPK/ERK, and mTORC1) following UDD, suggesting the activation of compensatory mechanisms to counteract muscle catabolism, in line with previous reports [10,11]. Importantly, MyoMed-205 prevented denervation-induced diaphragm fiber atrophy and enhanced gene expression of pathways associated with RNA processing, ribosome biogenesis, protein synthesis, and cell growth (e.g., Myc, Nr4a3, PI3K-Akt-mTOR, eIF4e), which is consistent with the evidences that MuRF1 can directly target ribosomal components and translation factors [16–18].

We previously have shown that MyoMed-205 increases Akt activation in the diaphragm under early UDD stress [6]. Herein, we further validated the MyoMed-205-mediated activation of the Akt-mTOR pathway at the protein level within 12 hours of UDD. Previous studies demonstrated that a murine MuRF1 gene knockout enhances Akt activation [26] and *de novo* protein synthesis. Thereby, MuRF1 KO mice seem less susceptible to muscle wasting [36]. Furthermore, MuRF1 can indirectly influence Myc activity by targeting Bin1, a negative regulator of Myc [18], which was found

significantly upregulated in MyoMed-205 treated rats. MyoMed-205 also enhanced NR4A3 gene expression, which positively regulates mTORC1 signaling and contributes to exercise-induced muscle hypertrophy [37]. Our data suggests that MyoMed-205 activates anabolic pathways at the gene and protein levels that might contribute to counteract UDD-associated diaphragm muscle atrophy.

Increased protein damage and breakdown also promote muscle wasting. In this study, we found a significant upregulation of inflammatory and proteolytic pathways (e.g., IL6-JAK-STAT3, TNFα/NFκB, ubiquitin-proteasome system) in the diaphragm after 12 hours of UDD. Noteworthy, animals treated with MyoMed-205 showed relatively higher gene expression of MuRF1 (i.e., TRIM63) compared with DNV_VEH, although not statistically significant, and without affecting protein levels. This may suggest a compensatory cellular mechanism in an attempt to enhance MuRF1 expression and/or activity following denervation, consistent with previous studies [38]. This finding underscores the importance of dose-response optimization, as excessive MyoMed-205 levels may disrupt muscle homeostasis and function, as we previously showed [6]. Conversely, we observed increased MuRF2 protein levels following 12 hours of UDD, a response abrogated by MyoMed-205, in line with previous studies suggesting that MuRF1 deletion/inhibition may downregulate MuRF2 expression, and that MyoMed-205 may also affect MuRF2 [22]. This effect may compromise MuRF1-MuRF2 heterodimerization and its cooperative role in myofibrillar protein ubiquitination [6,23,39]. Therefore, MyoMed-205-mediated protection against diaphragm fibers contractile dysfunction and atrophy might involve the disruption of MuRF1-MuRF2 cooperative role in myofibrillar breakdown.

Sustained cellular stress triggers myofiber apoptosis and diaphragm tissue remodeling, including intramuscular fat accumulation and fibrosis. Accordingly, we found upregulated transcription of adipogenic genes concomitantly with a higher number of ORO+ muscle cells with increased intracellular lipid content after 12 h of UDD. MyoMed-205 alleviated these effects, likely through downregulation of key adipogenic genes (e.g., Adiponectin, Pparγ). This might involve MyoMed-205 mediated blockade of MuRF2, known to suppress Pparγ expression/activity [40]. Furthermore, UDD enhanced gene expression linked to ECM collagen deposition and fibrosis, consistent with previous studies [13]. Notably, MyoMed-205 suppressed the denervation-induced ECM collagen deposition response at the transcriptional level. Previous experimental studies demonstrated that small-molecules targeting MuRF1 mitigate cardiac fibrosis, improving contractile function during heart failure [24]. Our data indicate that MyoMed-205 may contribute to the structural preservation of the diaphragm by mitigating denervation-induced intramuscular lipid accumulation and ECM collagen deposition triggered by UDD.

Study Limitations

This is the first study to provide mechanistic insights into how the small-molecule targeting MuRF1 (MyoMed-205) protects against early denervation-induced diaphragmatic dysfunction and atrophy in an experimental model. However, the following limitations must be considered: 1) These analyses were performed at a single time point (12 hours), limiting assessment of temporal dynamics in small-molecule targeting MuRF1 effects. 2) This study was limited to male rats treated with a single dosage (50 mg/kg bw), precluding assessment of potential sex-specific differences or dose-response relationships in response to denervation and MyoMed-

205 treatment. 3) Our mechanistic findings rely primarily on transcriptomic and protein content analyses, which do not account for important regulatory mechanisms such as post-transcriptional and post-translational modifications or changes in protein activity. 4) Cause-and-effect experiments were not feasible at this time to validate which mechanisms are crucial for small-molecule targeting MuRF1-mediated protection during early UDD. Future studies should employ multi-omics analyses, assess different dosage ranges in both sexes, and evaluate multiple time points to further comprehend the complex molecular mechanisms underlying small-molecule targeting MuRF1-mediated protection against denervation-induced diaphragm weakness and wasting.

Conclusion

The small-molecule targeting MuRF1, MyoMed-205, protects against denervation-induced diaphragm muscle contractile dysfunction and atrophy in rats undergoing 12 hours of UDD [6]. In this study, our mechanistic findings reveal that MyoMed-205 enhances the transcriptional mechanisms involved with the control of sarcomere structure and function, antioxidant defense, chaperone-mediated unfolded protein response, and muscle cell growth. MyoMed-205 also attenuated intramuscular lipid accumulation and pro-fibrotic responses triggered by UDD. These findings indicate MuRF1 as a promising therapeutic target for counteracting denervation-induced diaphragm muscle contractile dysfunction and atrophy.

Author's Contributions

FR and ASM were involved in the study's conceptualization. FR conducted animal experiments, sample collection, functional, morphometric, and molecular analysis.

PRJ conducted bioinformatic analysis (RNA-sequencing). FR and ASM performed data management and analysis. FR and ASM prepared the original manuscript. ASM and SL were involved in acquiring funding and project supervision. All authors were involved in the critical revision of the manuscript. All authors read and approved the final manuscript.

Acknowledgments

We wish to thank Kelly Patricia for her excellent laboratory technical assistance.

Funding

FR was supported by the São Paulo Research Foundation (FAPESP, grants 2020/04607-0 and 2022/14495-0). ASM was supported by FAPESP (grant 2022/16226-7) and the National Council for Scientific and Technological Development (CNPq, grant 305494/2022-8). PRJ was supported by Karolinska Institutet (KI) Research Foundation Grant. SL was supported by the German Centre for Cardiovascular Research (DZHK) partner site Mannheim-Heidelberg (grant SE-B42).

Ethical Standards Declaration

All animal studies have been approved by the appropriate ethics committee (CEUA ICB USP protocols #8728030320 and #5143091020), and have therefore been performed following the ethical standards laid down in the 1964 Declaration of Helsinki and its later amendments.

Conflict of Interest

Siegfried Labeit reports a patent filing for MyoMed-205 and further derivatives for its application to chronic muscle stress states (patent accession No WO2021023643A1). All other authors (Fernando Ribeiro, Paulo R. Jannig, and Anselmo S. Moriscot) declare no conflict of interest.

References

1. Fogarty MJ, Mantilla CB, Sieck GC. Breathing: Motor Control of Diaphragm Muscle. *Physiology* 2018;33:113–126.
2. McCool FD, Tzelepis GE. Dysfunction of the Diaphragm. *N Engl J Med* 2012;366:932–942.
3. Gransee HM, Mantilla CB, Sieck GC. Respiratory muscle plasticity. *Compr Physiol* 2012;2:1441–1462.
4. Sieck GC, Fogarty MJ. Diaphragm Muscle: A Pump That Can Not Fail. *Physiol Rev* 2025 doi:10.1152/physrev.00043.2024.
5. Shindoh C, Hida W, Kurosawa H, Ebihara S, Kikuchi Y, Takishima T *et al.* Effects of unilateral phrenic nerve denervation on diaphragm contractility in rat. *Tohoku J Exp Med* 1994;173:291–302.
6. Ribeiro F, Alves PKN, Bechara LRG, Ferreira JCB, Labeit S, Moriscot AS. Small-Molecule Inhibition of MuRF1 Prevents Early Disuse-Induced Diaphragmatic Dysfunction and Atrophy. *Int J Mol Sci* 2023;24:3637.
7. Gill LC, Ross HH, Lee KZ, Gonzalez-Rothi EJ, Dougherty BJ, Judge AR *et al.* Rapid diaphragm atrophy following cervical spinal cord hemisection. *Respir Physiol Neurobiol* 2014;192:66–73.
8. Gosselin LE, Brice G, Carlson B, Prakash YS, Sieck GC. Changes in satellite cell mitotic activity during acute period of unilateral diaphragm denervation. *J Appl Physiol* 1994;77:1128–1134.
9. Aravamudan B, Mantilla CB, Zhan WZ, Sieck GC. Denervation effects on myonuclear domain size of rat diaphragm fibers. *J Appl Physiol* 2006;100:1617–1622.
10. Argadine HM, Hellyer NJ, Mantilla CB, Zhan WZ, Sieck GC. The effect of denervation on protein synthesis and degradation in adult rat diaphragm muscle. *J Appl Physiol* 2009;107:438–444.
11. Argadine HM, Mantilla CB, Zhan WZ, Sieck GC. Intracellular signaling pathways regulating net protein balance following diaphragm muscle denervation. *Am J Physiol - Cell Physiol* 2011;300:318–327.
12. van der Pijl R, Strom J, Conijn S, Lindqvist J, Labeit S, Granzier H *et al.* Titin-based mechanosensing modulates muscle hypertrophy. *J Cachexia Sarcopenia Muscle* 2018;9:947–961.
13. Gosselin LE, Sieck GC, Aleff RA, Martinez DA, Vailas AC. Changes in diaphragm muscle collagen gene expression after acute unilateral denervation. *J Appl Physiol* 1995;79:1249–1254.
14. Centner T, Yano J, Kimura E, McElhinny AS, Pelin K, Witt CC *et al.* Identification of muscle specific ring finger proteins as potential regulators of the titin kinase domain. *J Mol Biol* 2001;306:717–726.
15. Bodine SC, Latres E, Baumhueter S, Lai VK-M, Clarke BA, Poueymirou WT *et al.* Identification of ubiquitin ligases required for skeletal muscle atrophy. *Science (80-)* 2001;294:1704–1708.
16. Witt SH, Granzier H, Witt CC, Labeit S. MURF-1 and MURF-2 target a specific subset of myofibrillar proteins redundantly: Towards understanding MURF-dependent muscle

ubiquitination. *J Mol Biol* 2005;350:713–722.
17. Witt CC, Witt SH, Lerche S, Labeit D, Back W, Labeit S. Cooperative control of striated muscle mass and metabolism by MuRF1 and MuRF2. *EMBO J* 2008;27:350–360.
18. Baehr LM, Hughes DC, Lynch SA, Van Haver D, Maia TM, Marshall AG *et al.* Identification of the MuRF1 Skeletal Muscle Ubiquitylome Through Quantitative Proteomics. *Function* 2021;2:1–18.
19. Peris-Moreno D, Taillandier D, Polge C. MuRF1/TRIM63, Master Regulator of Muscle Mass. *Int J Mol Sci* 2020;21:6663.
20. Hooijman PE, Beishuizen A, Witt CC, de Waard MC, Girbes ARJ, Spoelstra-de Man AME *et al.* Diaphragm muscle fiber weakness and ubiquitin–proteasome activation in critically ill patients. *Am J Respir Crit Care Med* 2015;191:1126–1138.
21. Liu J, Chen Y, Han D, Huang M. Inhibition of the expression of TRIM63 alleviates ventilator-induced diaphragmatic dysfunction by modulating the PPARα/PGC-1α pathway. *Mitochondrion* 2025;83:102025.
22. Bowen TS, Adams V, Werner S, Fischer T, Vinke P, Brogger MN *et al.* Small-molecule inhibition of MuRF1 attenuates skeletal muscle atrophy and dysfunction in cardiac cachexia. *J Cachexia Sarcopenia Muscle* 2017;8:939–953.
23. Adams V, Bowen TS, Werner S, Barthel P, Amberger C, Konzer A *et al.* Small-molecule-mediated chemical knock-down of MuRF1/MuRF2 and attenuation of diaphragm dysfunction in chronic heart failure. *J Cachexia Sarcopenia Muscle* 2019;10:1102–1115.
24. Adams V, Schauer A, Augstein A, Kirchhoff V, Draskowski R, Jannasch A *et al.* Targeting MuRF1 by small molecules in a HFpEF rat model improves myocardial diastolic function and skeletal muscle contractility. *J Cachexia Sarcopenia Muscle* 2022;13:1565–1581.
25. Adams V, Gußen V, Zozulya S, Cruz A, Moriscot A, Linke A *et al.* Small-Molecule Chemical Knockdown of MuRF1 in Melanoma Bearing Mice Attenuates Tumor Cachexia Associated Myopathy. *Cells* 2020;9:2272.
26. Labeit S, Hirner S, Bogomolovas J, Cruz A, Myrzabekova M, Moriscot A *et al.* Regulation of Glucose Metabolism by MuRF1 and Treatment of Myopathy in Diabetic Mice with Small Molecules Targeting MuRF1. *Int J Mol Sci* 2021;22:2225.
27. Matecki S, Dridi H, Jung B, Saint N, Reiken SR, Scheuermann V *et al.* Leaky ryanodine receptors contribute to diaphragmatic weakness during mechanical ventilation. *Proc Natl Acad Sci U S A* 2016;113:9069–9074.
28. Kiewitz R, Acklin C, Schäfer BW, Maco B, Uhrík B, Wuytack F *et al.* Ca2+-dependent interaction of S100A1 with the sarcoplasmic reticulum Ca2+-ATPase2a and phospholamban in the human heart. *Biochem Biophys Res Commun* 2003;306:550–557.
29. Most P, Bernotat J, Ehlermann P, Pleger ST, Reppel M, Börries M *et al.* S100A1: A regulator of myocardial contractility. *Proc Natl Acad Sci* 2001;98:13889–13894.
30. Shanely RA, Zergeroglu MA, Lennon SL, Sugiura T, Yimlamai T, Enns D *et al.* Mechanical ventilation–induced diaphragmatic atrophy Is associated with oxidative injury and increased proteolytic activity. *Am J Respir Crit Care Med* 2002;166:1369–1374.
31. Martin TG, Myers VD, Dubey P, Dubey S, Perez E, Moravec CS *et al.* Cardiomyocyte contractile impairment in heart failure results from reduced BAG3-mediated sarcomeric protein turnover. *Nat Commun* 2021;12:2942.
32. Meister-Broekema M, Freilich R, Jagadeesan C, Rauch JN, Bengoechea R, Motley WW *et al.* Myopathy associated BAG3 mutations lead to protein aggregation by stalling Hsp70 networks. *Nat Commun* 2018;9:5342.
33. Salah H, Li M, Cacciani N, Gastaldello S, Ogilvie H, Akkad H *et al.* The chaperone co-inducer BGP-15 alleviates ventilation-induced diaphragm dysfunction. *Sci Transl Med* 2016;8:350ra103.
34. Geiger PC, Cody MJ, Macken RL, Bayrd ME, Sieck GC. Effect of unilateral

denervation on maximum specific force in rat diaphragm muscle fibers. *J Appl Physiol* 2001;90:1196–1204.
35. Welvaart WN, Paul MA, van Hees HWH, Stienen GJM, Niessen JWM, de Man FS *et al.* Diaphragm muscle fiber function and structure in humans with hemidiaphragm paralysis. *Am J Physiol - Lung Cell Mol Physiol* 2011;301:228–235.
36. Koyama S, Hata S, Witt CC, Ono Y, Lerche S, Ojima K *et al.* Muscle RING-Finger Protein-1 (MuRF1) as a connector of muscle energy metabolism and protein synthesis. *J Mol Biol* 2008;376:1224–1236.
37. Pillon NJ, Gabriel BM, Dollet L, Smith JAB, Sardón Puig L, Botella J *et al.* Transcriptomic profiling of skeletal muscle adaptations to exercise and inactivity. *Nat Commun* 2020;11:470.
38. Furlow JD, Watson ML, Waddell DS, Neff ES, Baehr LM, Ross AP *et al.* Altered gene expression patterns in muscle ring finger 1 null mice during denervation- and dexamethasone-induced muscle atrophy. *Physiol Genomics* 2013;45:1168–1185.
39. Nguyen T, Bowen TS, Augstein A, Schauer A, Gasch A, Linke A *et al.* Expression of MuRF1 or MuRF2 is essential for the induction of skeletal muscle atrophy and dysfunction in a murine pulmonary hypertension model. *Skelet Muscle* 2020;10:1–10.
40. He J, Quintana MT, Sullivan J, L Parry T, J Grevengoed T, Schisler JC *et al.* MuRF2 regulates PPARγ1 activity to protect against diabetic cardiomyopathy and enhance weight gain induced by a high fat diet. *Cardiovasc Diabetol* 2015;14:97.

Table Legend

Table 1. Differentially expressed genes (DEGs) altered by MyoMed-205 treatment compared with vehicle after 12 hours of UDD.

From the 69 DEGs identified in DNV_205 vs. DNV_VEH listed above, 7 DEGs were upregulated (UP), while other 62 DEGs were downregulated (DOWN) in DNV_205 compared with DNV_VEH group. The DEGs are presented as UP and DOWN categories and ranked according to the highest to lowest fold change value. lfcSE, log fold change standard error), Padj, adjusted p-value.

Figure Legends

Figure 1. Transcriptomic profiling of the diaphragm following 12 h of unilateral diaphragm denervation (UDD) and identification of pathways responsive to MyoMed-205. (A) Schematic illustration of the experimental design used to investigate the effect of small-molecule targeting MuRF1 (MyoMed-205, 50 mg/kg bw, intravenous delivery) upon early UDD pathophysiology in rats. (B) Principal component analysis for RNA-seq of diaphragm muscle and identification of differentially expressed genes (DEGs, Padj < 0.05) across the distinct experimental conditions (n = 4 per group). Upregulated genes are represented in red, while downregulated genes are represented in blue. (C) Hierarchical clustered heat map highlights five clusters of DEGs identified in response to UDD and MyoMed-205 compared with the control. (D) Gene Set Enrichment Analysis (GSEA) reveals the hallmark pathways responsive to UDD and the impacts of MyoMed-205. Additionally, GSEA indicates the altered (E) molecular functions (GOMF) and (F) cellular compartments (GOCC) of the diaphragm muscle in response to UDD and MyoMed-205 compared with controls. Padj, adjusted p-value. FDR, false discovery rate.

Figure 2. MyoMed-205 protects against diaphragm fiber atrophy induced by 12 hours of unilateral diaphragm denervation (UDD). (A) Representative photomicrographs of diaphragm muscle immunolabeled with antibodies against the myosin heavy chain (MyHC) isoforms, type I (violet), type IIa (light blue), type IIb/x (black), and dystrophin (white) for morphometric analysis by fiber type. Scale bar = 100 μm. (B) Fibers' cross-sectional area (CSA), relative CSA percentual change compared with Sham-controls, and relative percentual distribution by fiber type. Data are presented as mean and standard deviation (n = 8). One-way ANOVA followed by Tukey's post-hoc test was used for statistical comparisons among the groups. *, $p < 0.05$. (C) Heat map of genes linked to muscle contraction (i.e., synaptic vesicle membrane and contractile fiber). (D) Heat map of genes linked to sarcomere structure and function (i.e., actin filament, I band, and dystrophin glycoprotein complex (DCG)). (F) Protein levels of calcium-handling markers were assessed by Western blotting. Data are presented as mean and standard deviation of the fold change relative to the control group (n = 7 to 8). One-way ANOVA followed by Tukey's post-hoc test was used for statistical comparisons among the groups. *, $p < 0.05$.

Figure 3. Unilateral diaphragm denervation (UDD) enhances transcriptional activation of pathways associated with mitochondrial dysfunction and oxidative stress, while MyoMed-205 upregulates the gene expression of antioxidant factors. (A) Heat map of genes involved in the control of mitochondrial biogenesis and dynamics. (B-C) Heat map of genes associated with mitochondrial structural and functional complexes. (D) Heat map of genes linked to mitochondrial energy production and metabolism. (E)

Heat map of genes involved with reactive oxygen species (ROS) production and antioxidant response.

Figure 4. MyoMed-205 enhances the activation of signaling pathways controlling ribosome biogenesis, protein synthesis, and cell growth. (A) Heat map of Myc target genes. (B) Heat map of genes associated with the PI3K-AKT-mTOR pathway. (C) Heat map of genes controlling ribosome biogenesis and translation initiation. (D) Protein levels of MAPK and PI3K-Akt-mTOR pathways markers were assessed by Western blotting. Data are presented as mean and standard deviation of the fold change relative to the control group (n = 6 to 7). One-way ANOVA followed by Tukey's post-hoc test was used for statistical comparisons among the groups. *, $p < 0.05$; **, $p < 0.01$.

Figure 5. MyoMed-205 enhances the transcriptional activation of heat shock chaperones and the unfolded protein response (UPR) mechanism in the diaphragm under denervation-induced cellular stress and catabolic state. (A) Heat map of genes from the IL6-JAK-STAT3 pathway. (B) Heat map of genes associated with the chaperone complex and UPR. (C) Heat map of genes linked to the ubiquitin-proteasome system. (D) Protein levels of ubiquitin-proteasome pathway markers were assessed by Western blotting. Data are presented as mean and standard deviation of the fold change relative to the control group (n = 8). One-way ANOVA followed by Tukey's post-hoc test was used for statistical comparisons among the groups. *, $p < 0.05$; **, $p < 0.01$. (E) Heat maps of genes from the p53 pathway. (F) Heat maps of genes associated with apoptosis.

Figure 6. MyoMed-205 attenuates denervation-induced intramuscular fat accumulation in the diaphragm by downregulating pro-adipogenic genes. (A) Heat map of genes related to adipogenesis and intramuscular lipid accumulation. (B) Protein levels of adipogenesis pathway markers were assessed by Western blotting. Data are presented as mean and standard deviation of the fold change relative to the control group (n = 8). One-way ANOVA followed by Tukey's post-hoc test was used for statistical comparisons among the groups. (C) Representative photomicrographs of Oil Red O (ORO) staining of the diaphragm for assessing intramuscular lipid accumulation following 12 h of unilateral diaphragm denervation and the effects of MyoMed-205. Scale bar = 50 μm. (D) Quantitative analysis of positive ORO muscle cells (i.e., intracellular lipid droplet area > 5% of total muscle fiber area). (E) Mean intracellular lipid droplet area of diaphragm muscle fibers < 2500 μm^2 (predominantly oxidative metabolism) and fibers > 2500 μm^2 (predominantly glycolytic metabolism). In total, 300 muscle cells were assessed per sample to estimate the average positive ORO cells and intracellular lipid content. Data are presented as mean and standard deviation (n = 7). One-way ANOVA followed by Tukey's post-hoc test was used for statistical comparisons among the groups. *, $p < 0.05$; **, $p < 0.01$.

Figure 7. MyoMed-205 mitigates denervation-induced upregulation of genes involved with extracellular matrix collagen deposition and fibrosis in the diaphragm at the transcriptional level. (A) Heat map of genes involved in the formation of collagen trimmers. (B) Heat map of genes associated with the basement membrane. (C) Heat map of genes associated with collagen assembly and the extracellular matrix.

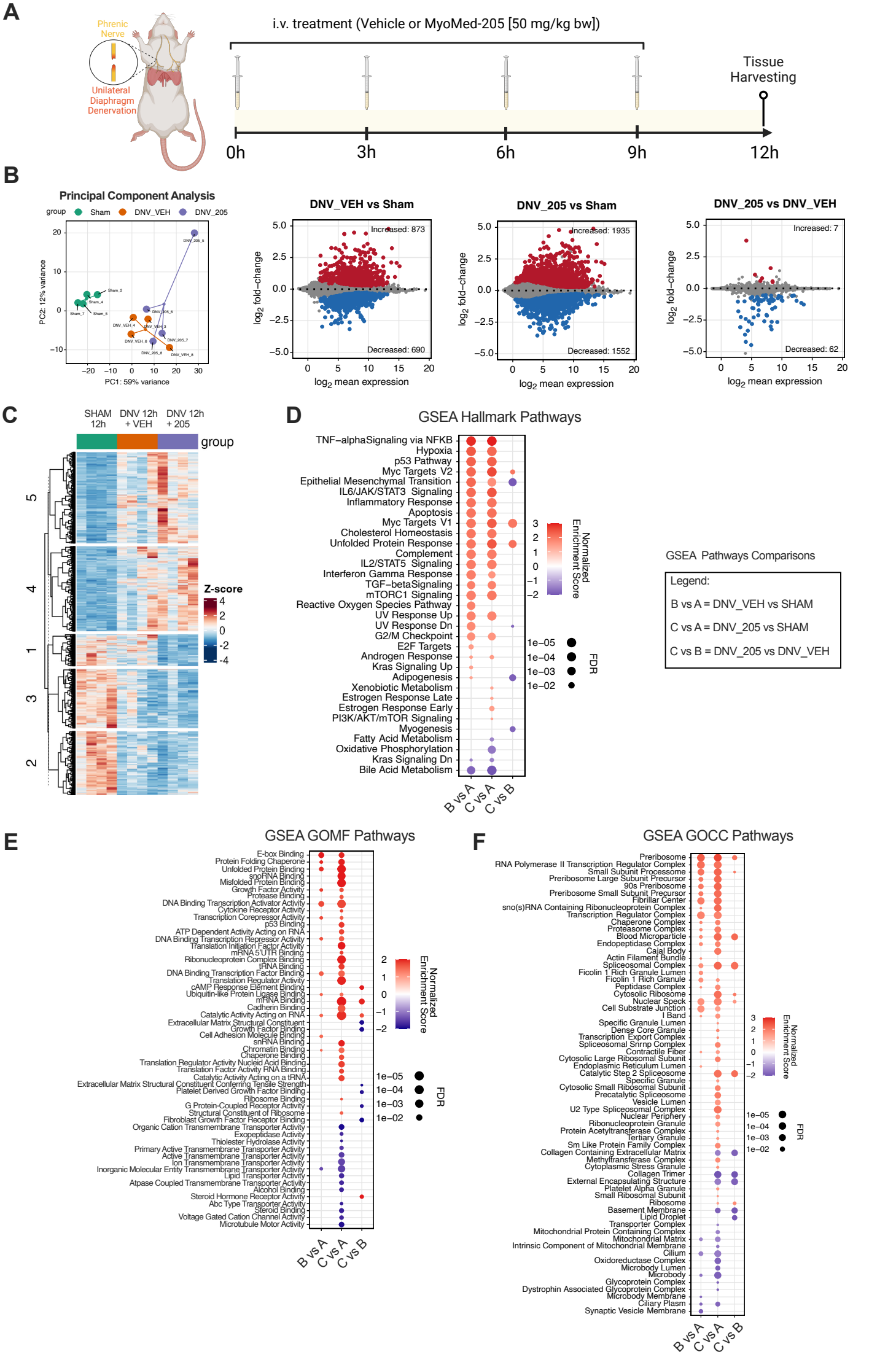
A
Phrenic Nerve
Unilateral Diaphragm Denervation
i.v. treatment (Vehicle or MyoMed-205 [50 mg/kg bw])
Tissue Harvesting
0h
3h
6h
9h
12h
B
Principal Component Analysis
group Sham DNV_VEH DNV_205
PC2: 12% variance
PC1: 59% variance
DNV_VEH vs Sham
Increased: 873
Decreased: 690
DNV_205 vs Sham
Increased: 1935
Decreased: 1552
DNV_205 vs DNV_VEH
Increased: 7
Decreased: 62
log2 fold-change
log2 mean expression
C
SHAM 12h
DNV 12h + VEH
DNV 12h + 205
group
Z-score
D
GSEA Hallmark Pathways
TNF-alphaSignaling via NFKB
Hypoxia
p53 Pathway
Myc Targets V2
Epithelial Mesenchymal Transition
IL6/JAK/STAT3 Signaling
Inflammatory Response
Apoptosis
Myc Targets V1
Cholesterol Homeostasis
Unfolded Protein Response
Complement
IL2/STAT5 Signaling
Interferon Gamma Response
TGF-betaSignaling
mTORC1 Signaling
Reactive Oxygen Species Pathway
UV Response Up
UV Response Dn
G2/M Checkpoint
E2F Targets
Androgen Response
Kras Signaling Up
Adipogenesis
Xenobiotic Metabolism
Estrogen Response Late
Estrogen Response Early
PI3K/AKT/mTOR Signaling
Myogenesis
Fatty Acid Metabolism
Oxidative Phosphorylation
Kras Signaling Dn
Bile Acid Metabolism
B vs A
C vs A
C vs B
Normalized Enrichment Score
FDR
GSEA Pathways Comparisons
Legend:
B vs A = DNV_VEH vs SHAM
C vs A = DNV_205 vs SHAM
C vs B = DNV_205 vs DNV_VEH
E
GSEA GOMF Pathways
F
GSEA GOCC Pathways

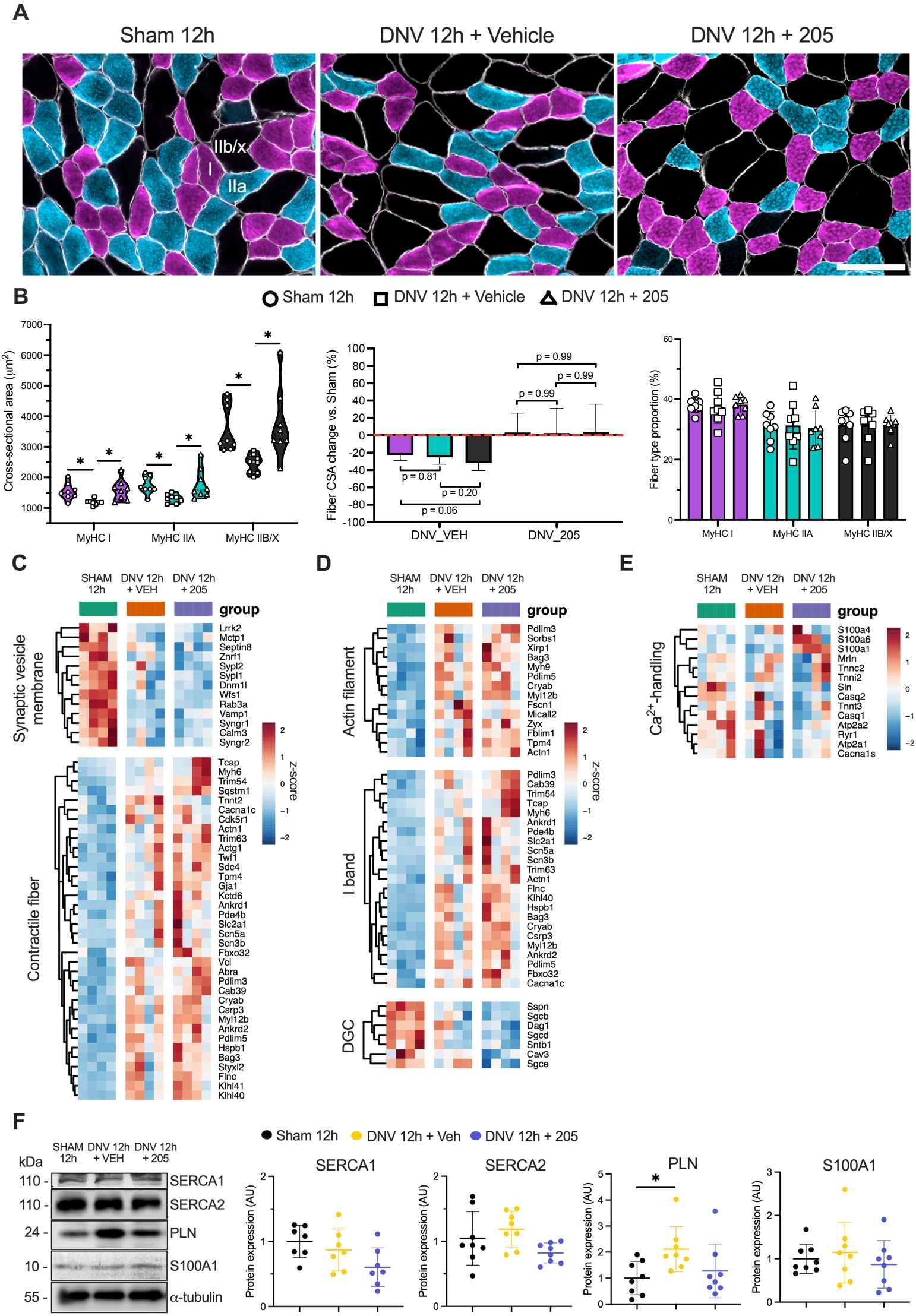
A
Sham 12h
DNV 12h + Vehicle
DNV 12h + 205
IIb/x
I
IIa
B
Sham 12h
DNV 12h + Vehicle
DNV 12h + 205
Cross-sectional area (μm²)
MyHC I
MyHC IIA
MyHC IIB/X
Fiber CSA change vs. Sham (%)
p = 0.81
p = 0.20
p = 0.06
p = 0.99
DNV_VEH
DNV_205
Fiber type proportion (%)
C
SHAM 12h
DNV 12h + VEH
DNV 12h + 205
group
Synaptic vesicle membrane
Lrrk2
Mctp1
Septin8
Znrf1
Sypl2
Sypl1
Dnm1l
Wfs1
Rab3a
Vamp1
Syngr1
Calm3
Syngr2
Contractile fiber
Tcap
Myh6
Trim54
Sqstm1
Tnnt2
Cacna1c
Cdk5r1
Actn1
Trim63
Actg1
Twf1
Sdc4
Tpm4
Gja1
Kctd6
Ankrd1
Pde4b
Slc2a1
Scn5a
Scn3b
Fbxo32
Vcl
Abra
Pdlim3
Cab39
Cryab
Csrp3
Myl12b
Ankrd2
Pdlim5
Hspb1
Bag3
Styxl2
Flnc
Klhl41
Klhl40
z-score
D
Actin filament
Pdlim3
Sorbs1
Xirp1
Bag3
Myh9
Pdlim5
Cryab
Myl12b
Fscn1
Micall2
Zyx
Fblim1
Tpm4
Actn1
I band
Pdlim3
Cab39
Trim54
Tcap
Myh6
Ankrd1
Pde4b
Slc2a1
Scn5a
Scn3b
Trim63
Actn1
Flnc
Klhl40
Hspb1
Bag3
Cryab
Csrp3
Myl12b
Ankrd2
Pdlim5
Fbxo32
Cacna1c
DGC
Sspn
Sgcb
Dag1
Sgcd
Sntb1
Cav3
Sgce
E
Ca2+-handling
S100a4
S100a6
S100a1
Mrln
Tnnc2
Tnni2
Sln
Casq2
Tnnt3
Casq1
Atp2a2
Ryr1
Atp2a1
Cacna1s
F
kDa
SHAM 12h
DNV 12h + VEH
DNV 12h + 205
110 -
SERCA1
110 -
SERCA2
24 -
PLN
10 -
S100A1
55 -
α-tubulin
Sham 12h
DNV 12h + Veh
DNV 12h + 205
SERCA1
SERCA2
PLN
S100A1
Protein expression (AU)

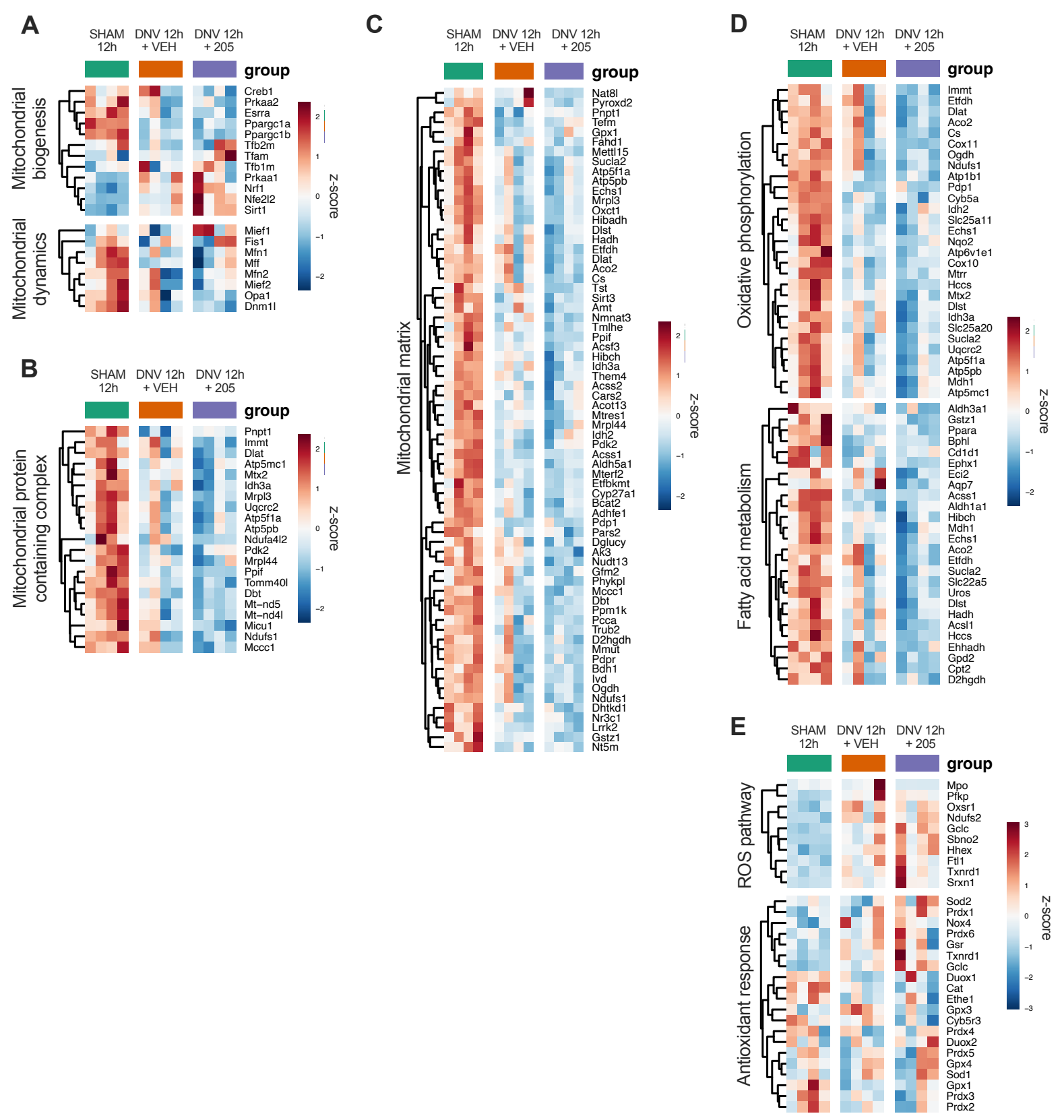
A
SHAM 12h
DNV 12h + VEH
DNV 12h + 205
group
Mitochondrial biogenesis
Creb1
Prkaa2
Esrra
Ppargc1a
Ppargc1b
Tfb2m
Tfam
Tfb1m
Prkaa1
Nrf1
Nfe2l2
Sirt1
Mitochondrial dynamics
Mief1
Fis1
Mfn1
Mff
Mfn2
Mief2
Opa1
Dnm1l
z-score
2
1
0
−1
−2
B
SHAM 12h
DNV 12h + VEH
DNV 12h + 205
group
Mitochondrial protein containing complex
Pnpt1
Immt
Dlat
Atp5mc1
Mtx2
Idh3a
Mrpl3
Uqcrc2
Atp5f1a
Atp5pb
Ndufa4l2
Pdk2
Mrpl44
Ppif
Tomm40l
Dbt
Mt−nd5
Mt−nd4l
Micu1
Ndufs1
Mccc1
z-score
2
1
0
−1
−2
C
SHAM 12h
DNV 12h + VEH
DNV 12h + 205
group
Mitochondrial matrix
Nat8l
Pyroxd2
Pnpt1
Tefm
Gpx1
Fahd1
Mettl15
Sucla2
Atp5f1a
Atp5pb
Echs1
Mrpl3
Oxct1
Hibadh
Dlst
Hadh
Etfdh
Dlat
Aco2
Cs
Tst
Sirt3
Amt
Nmnat3
Tmlhe
Ppif
Acsf3
Hibch
Idh3a
Them4
Acss2
Cars2
Acot13
Mtres1
Mrpl44
Idh2
Pdk2
Acss1
Aldh5a1
Mterf2
Etfbkmt
Cyp27a1
Bcat2
Adhfe1
Pdp1
Pars2
Dglucy
Ak3
Nudt13
Gfm2
Phykpl
Mccc1
Dbt
Ppm1k
Pcca
Trub2
D2hgdh
Mmut
Pdpr
Bdh1
Ivd
Ogdh
Ndufs1
Dhtkd1
Nr3c1
Lrrk2
Gstz1
Nt5m
z-score
2
1
0
−1
−2
D
SHAM 12h
DNV 12h + VEH
DNV 12h + 205
group
Oxidative phosphorylation
Immt
Etfdh
Dlat
Aco2
Cs
Cox11
Ogdh
Ndufs1
Atp1b1
Pdp1
Cyb5a
Idh2
Slc25a11
Echs1
Nqo2
Atp6v1e1
Cox10
Mtrr
Hccs
Mtx2
Dlst
Idh3a
Slc25a20
Sucla2
Uqcrc2
Atp5f1a
Atp5pb
Mdh1
Atp5mc1
Fatty acid metabolism
Aldh3a1
Gstz1
Ppara
Bphl
Cd1d1
Ephx1
Eci2
Aqp7
Acss1
Aldh1a1
Hibch
Mdh1
Echs1
Aco2
Etfdh
Sucla2
Slc22a5
Uros
Dlst
Hadh
Acsl1
Hccs
Ehhadh
Gpd2
Cpt2
D2hgdh
z-score
2
1
0
−1
−2
E
SHAM 12h
DNV 12h + VEH
DNV 12h + 205
group
ROS pathway
Mpo
Pfkp
Oxsr1
Ndufs2
Gclc
Sbno2
Hhex
Ftl1
Txnrd1
Srxn1
Antioxidant response
Sod2
Prdx1
Nox4
Prdx6
Gsr
Txnrd1
Gclc
Duox1
Cat
Ethe1
Gpx3
Cyb5r3
Prdx4
Duox2
Prdx5
Gpx4
Sod1
Gpx1
Prdx3
Prdx2
z-score
3
2
1
0
−1
−2
−3

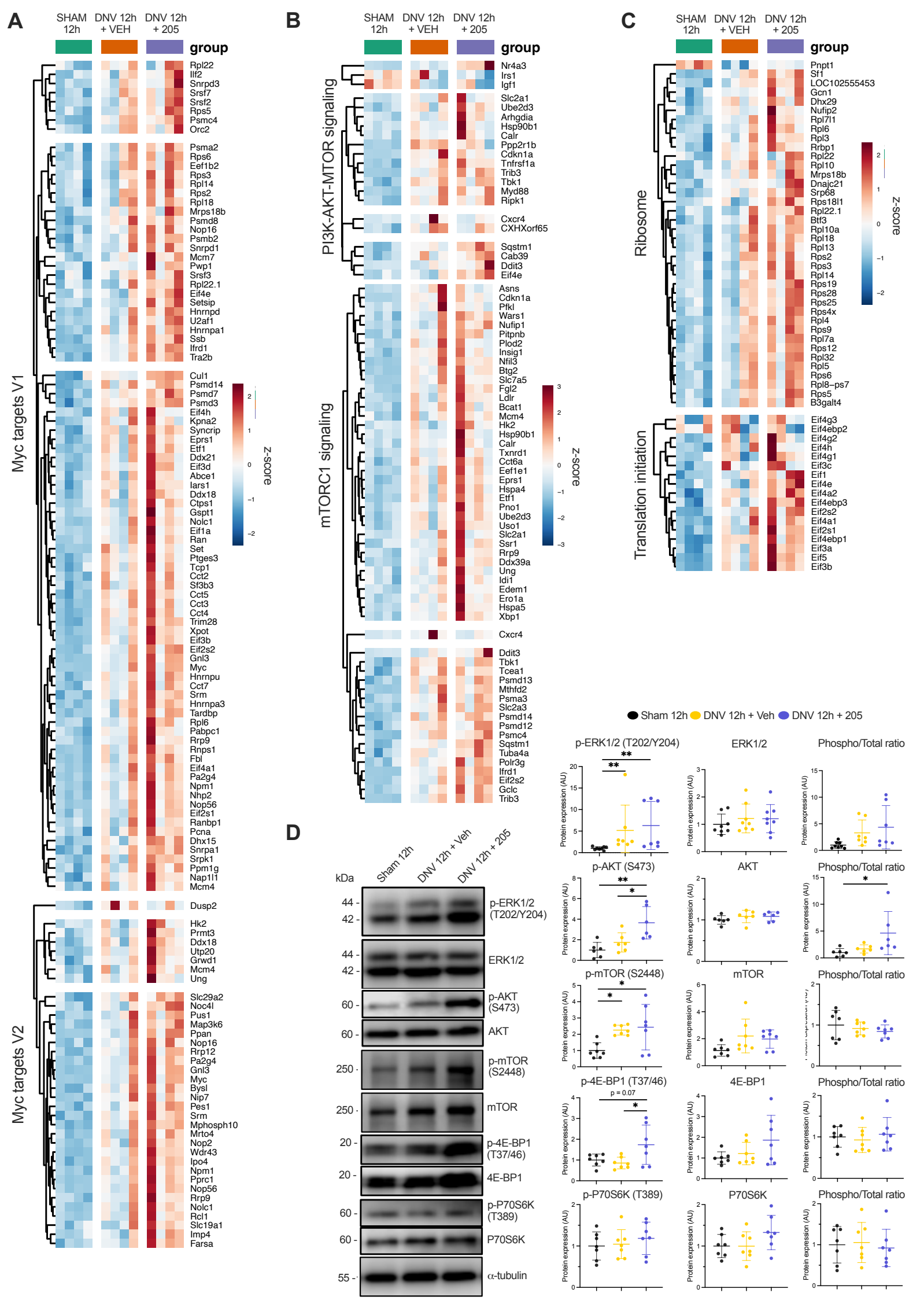
A
SHAM 12h
DNV 12h + VEH
DNV 12h + 205
group
Myc targets V1
Rpl22
Ilf2
Snrpd3
Srsf7
Srsf2
Rps5
Psmc4
Orc2
Psma2
Rps6
Eef1b2
Rps3
Rpl14
Rps2
Rpl18
Mrps18b
Psmd8
Nop16
Psmb2
Snrpd1
Mcm7
Pwp1
Srsf3
Rpl22.1
Eif4e
Setsip
Hnrnpd
U2af1
Hnrnpa1
Ssb
Ifrd1
Tra2b
Cul1
Psmd14
Psmd7
Psmd3
Eif4h
Kpna2
Syncrip
Eprs1
Etf1
Ddx21
Eif3d
Abce1
Iars1
Ddx18
Ctps1
Gspt1
Nolc1
Eif1a
Ran
Set
Ptges3
Tcp1
Cct2
Sf3b3
Cct5
Cct3
Cct4
Trim28
Xpot
Eif3b
Eif2s2
Gnl3
Myc
Hnrnpu
Cct7
Srm
Hnrnpa3
Tardbp
Rpl6
Pabpc1
Rrp9
Rnps1
Fbl
Eif4a1
Pa2g4
Npm1
Nhp2
Nop56
Eif2s1
Ranbp1
Pcna
Dhx15
Snrpa1
Srpk1
Ppm1g
Nap1l1
Mcm4
Dusp2
Myc targets V2
Hk2
Prmt3
Ddx18
Utp20
Grwd1
Mcm4
Ung
Slc29a2
Noc4l
Pus1
Map3k6
Ppan
Nop16
Rrp12
Pa2g4
Gnl3
Myc
Bysl
Nip7
Pes1
Srm
Mphosph10
Mrto4
Nop2
Wdr43
Ipo4
Npm1
Pprc1
Nop56
Rrp9
Nolc1
Rcl1
Slc19a1
Imp4
Farsa
z-score
B
PI3K-AKT-MTOR signaling
Nr4a3
Irs1
Igf1
Slc2a1
Ube2d3
Arhgdia
Hsp90b1
Calr
Ppp2r1b
Cdkn1a
Tnfrsf1a
Trib3
Tbk1
Myd88
Ripk1
Cxcr4
CXHXorf65
Sqstm1
Cab39
Ddit3
Eif4e
mTORC1 signaling
Asns
Cdkn1a
Pfkl
Wars1
Nufip1
Pitpnb
Plod2
Insig1
Nfil3
Btg2
Slc7a5
Fgl2
Ldlr
Bcat1
Mcm4
Hk2
Hsp90b1
Calr
Txnrd1
Cct6a
Eef1e1
Eprs1
Hspa4
Etf1
Pno1
Ube2d3
Uso1
Slc2a1
Ssr1
Rrp9
Ddx39a
Ung
Idi1
Edem1
Ero1a
Hspa5
Xbp1
Cxcr4
Ddit3
Tbk1
Tcea1
Psmd13
Mthfd2
Psma3
Slc2a3
Psmd14
Psmd12
Psmc4
Sqstm1
Tuba4a
Polr3g
Ifrd1
Eif2s2
Gclc
Trib3
z-score
C
Ribosome
Pnpt1
Sf1
LOC102555453
Gcn1
Dhx29
Nufip2
Rpl7l1
Rpl6
Rpl3
Rrbp1
Rpl22
Rpl10
Mrps18b
Dnajc21
Srp68
Rps18l1
Rpl22.1
Btf3
Rpl10a
Rpl18
Rpl13
Rps2
Rps3
Rpl14
Rps19
Rps28
Rps25
Rps4x
Rpl4
Rps9
Rpl7a
Rps12
Rpl32
Rpl5
Rps6
Rpl8–ps7
Rps5
B3galt4
Translation initiation
Eif4g3
Eif4ebp2
Eif4g2
Eif4h
Eif4g1
Eif3c
Eif1
Eif4e
Eif4a2
Eif4ebp3
Eif2s2
Eif4a1
Eif2s1
Eif4ebp1
Eif3a
Eif5
Eif3b
z-score
D
kDa
Sham 12h
DNV 12h + Veh
DNV 12h + 205
44
42
p-ERK1/2 (T202/Y204)
ERK1/2
60
p-AKT (S473)
AKT
250
p-mTOR (S2448)
mTOR
20
p-4E-BP1 (T37/46)
4E-BP1
p-P70S6K (T389)
P70S6K
55
α-tubulin
Sham 12h
DNV 12h + Veh
DNV 12h + 205
p-ERK1/2 (T202/Y204)
ERK1/2
Phospho/Total ratio
p-AKT (S473)
AKT
Phospho/Total ratio
p-mTOR (S2448)
mTOR
Phospho/Total ratio
p-4E-BP1 (T37/46)
p = 0.07
4E-BP1
Phospho/Total ratio
p-P70S6K (T389)
P70S6K
Phospho/Total ratio
Protein expression (AU)

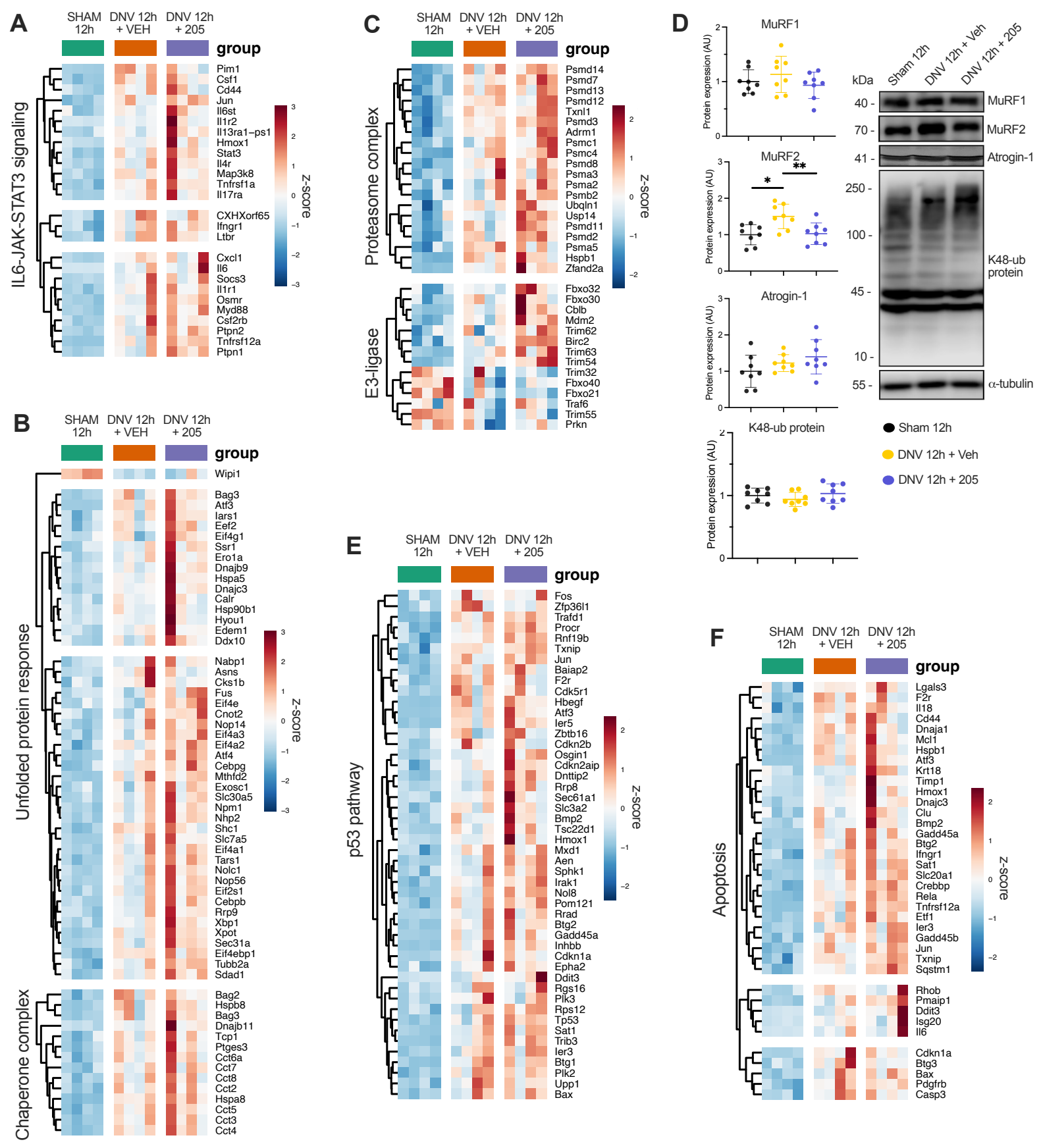
A
SHAM 12h
DNV 12h + VEH
DNV 12h + 205
group
IL6-JAK-STAT3 signaling
Pim1
Csf1
Cd44
Jun
Il6st
Il1r2
Il13ra1−ps1
Hmox1
Stat3
Il4r
Map3k8
Tnfrsf1a
Il17ra
CXHXorf65
Ifngr1
Ltbr
Cxcl1
Il6
Socs3
Il1r1
Osmr
Myd88
Csf2rb
Ptpn2
Tnfrsf12a
Ptpn1
z-score
B
Unfolded protein response
Wipi1
Bag3
Atf3
Iars1
Eef2
Eif4g1
Ssr1
Ero1a
Dnajb9
Hspa5
Dnajc3
Calr
Hsp90b1
Hyou1
Edem1
Ddx10
Nabp1
Asns
Cks1b
Fus
Eif4e
Cnot2
Nop14
Eif4a3
Eif4a2
Atf4
Cebpg
Mthfd2
Exosc1
Slc30a5
Npm1
Nhp2
Shc1
Slc7a5
Eif4a1
Tars1
Nolc1
Nop56
Eif2s1
Cebpb
Rrp9
Xbp1
Xpot
Sec31a
Eif4ebp1
Tubb2a
Sdad1
Chaperone complex
Bag2
Hspb8
Bag3
Dnajb11
Tcp1
Ptges3
Cct6a
Cct7
Cct8
Cct2
Hspa8
Cct5
Cct3
Cct4
C
Proteasome complex
Psmd14
Psmd7
Psmd13
Psmd12
Txnl1
Psmd3
Adrm1
Psmc1
Psmc4
Psmd8
Psma3
Psma2
Psmb2
Ubqln1
Usp14
Psmd11
Psmd2
Psma5
Hspb1
Zfand2a
E3-ligase
Fbxo32
Fbxo30
Cblb
Mdm2
Trim62
Birc2
Trim63
Trim54
Trim32
Fbxo40
Fbxo21
Traf6
Trim55
Prkn
D
MuRF1
MuRF2
Atrogin-1
K48-ub protein
Protein expression (AU)
kDa
Sham 12h
DNV 12h + Veh
DNV 12h + 205
40 -
70 -
41 -
250 -
100 -
45 -
10 -
55 -
α-tubulin
E
p53 pathway
Fos
Zfp36l1
Trafd1
Procr
Rnf19b
Txnip
Jun
Baiap2
F2r
Cdk5r1
Hbegf
Atf3
Ier5
Zbtb16
Cdkn2b
Osgin1
Cdkn2aip
Dnttip2
Rrp8
Sec61a1
Slc3a2
Bmp2
Tsc22d1
Hmox1
Mxd1
Aen
Sphk1
Irak1
Nol8
Pom121
Rrad
Btg2
Gadd45a
Inhbb
Cdkn1a
Epha2
Ddit3
Rgs16
Plk3
Rps12
Tp53
Sat1
Trib3
Ier3
Btg1
Plk2
Upp1
Bax
F
Apoptosis
Lgals3
F2r
Il18
Cd44
Dnaja1
Mcl1
Hspb1
Atf3
Krt18
Timp1
Hmox1
Dnajc3
Clu
Bmp2
Gadd45a
Btg2
Ifngr1
Sat1
Slc20a1
Crebbp
Rela
Tnfrsf12a
Etf1
Ier3
Gadd45b
Jun
Txnip
Sqstm1
Rhob
Pmaip1
Ddit3
Isg20
Il6
Cdkn1a
Btg3
Bax
Pdgfrb
Casp3

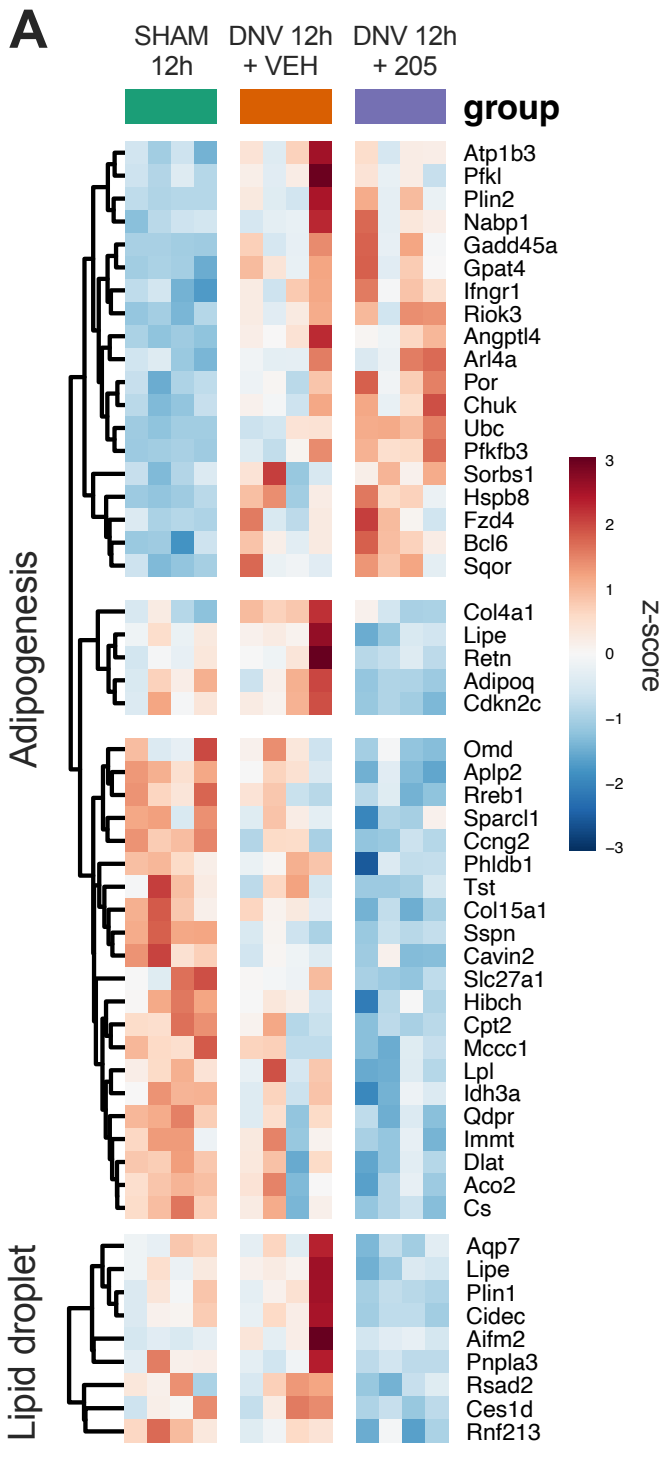
A
SHAM 12h
DNV 12h + VEH
DNV 12h + 205
group
Adipogenesis
Lipid droplet
Atp1b3
Pfkl
Plin2
Nabp1
Gadd45a
Gpat4
Ifngr1
Riok3
Angptl4
Arl4a
Por
Chuk
Ubc
Pfkfb3
Sorbs1
Hspb8
Fzd4
Bcl6
Sqor
Col4a1
Lipe
Retn
Adipoq
Cdkn2c
Omd
Aplp2
Rreb1
Sparcl1
Ccng2
Phldb1
Tst
Col15a1
Sspn
Cavin2
Slc27a1
Hibch
Cpt2
Mccc1
Lpl
Idh3a
Qdpr
Immt
Dlat
Aco2
Cs
Aqp7
Lipe
Plin1
Cidec
Aifm2
Pnpla3
Rsad2
Ces1d
Rnf213
Z-score
3
2
1
0
−1
−2
−3

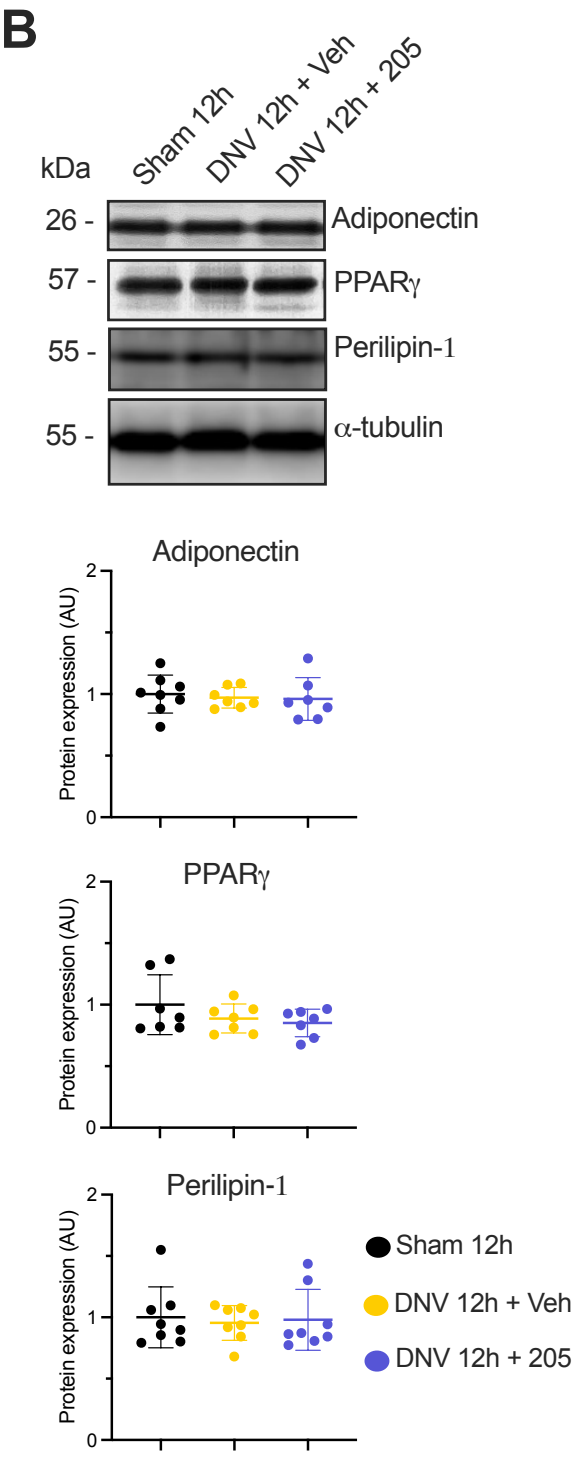
B
kDa
Sham 12h
DNV 12h + Veh
DNV 12h + 205
26 -
Adiponectin
57 -
PPARγ
55 -
Perilipin-1
55 -
α-tubulin
Adiponectin
PPARγ
Perilipin-1
Protein expression (AU)
Sham 12h
DNV 12h + Veh
DNV 12h + 205

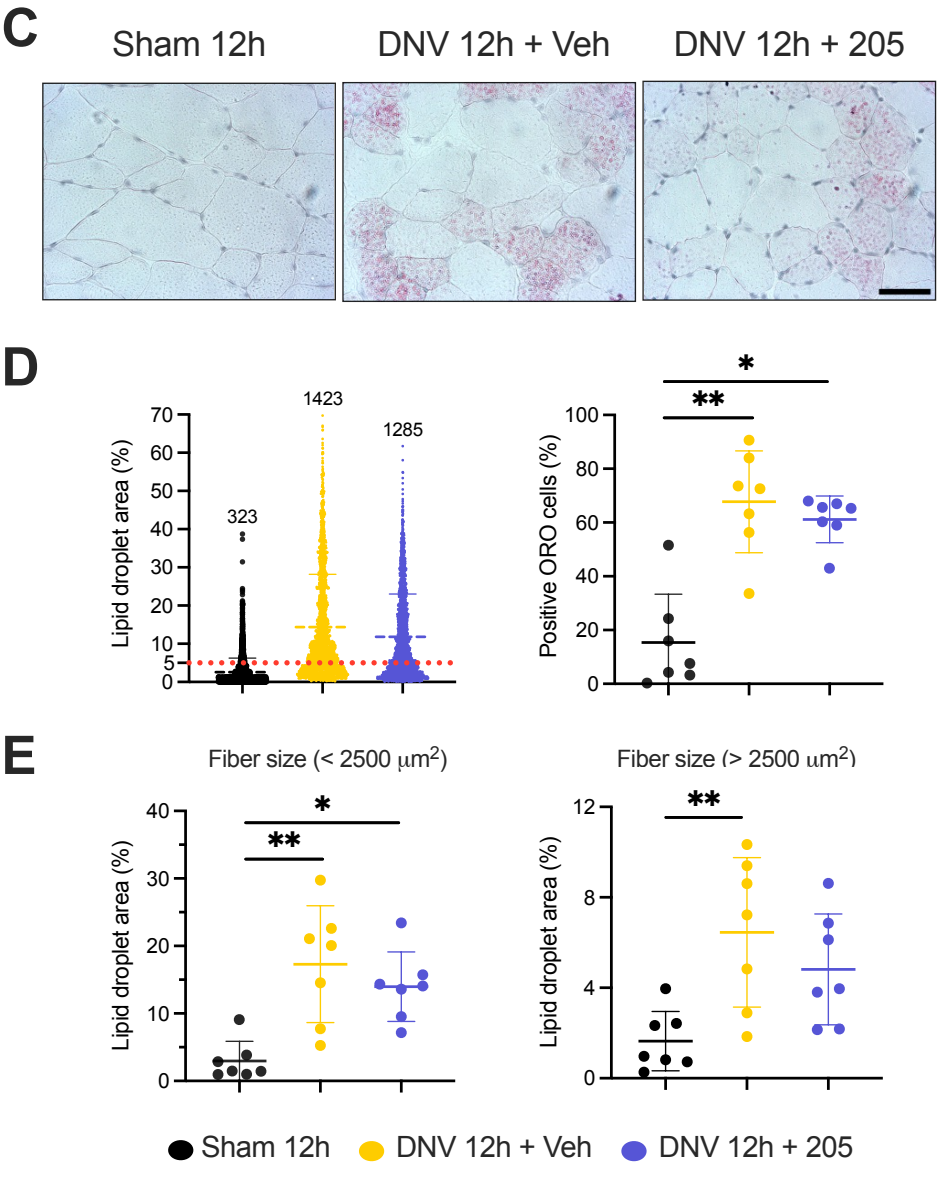
C
Sham 12h
DNV 12h + Veh
DNV 12h + 205
D
Lipid droplet area (%)
323
1423
1285
Positive ORO cells (%)
E
Fiber size (< 2500 μm²)
Fiber size (> 2500 um²)
Lipid droplet area (%)
Sham 12h
DNV 12h + Veh
DNV 12h + 205

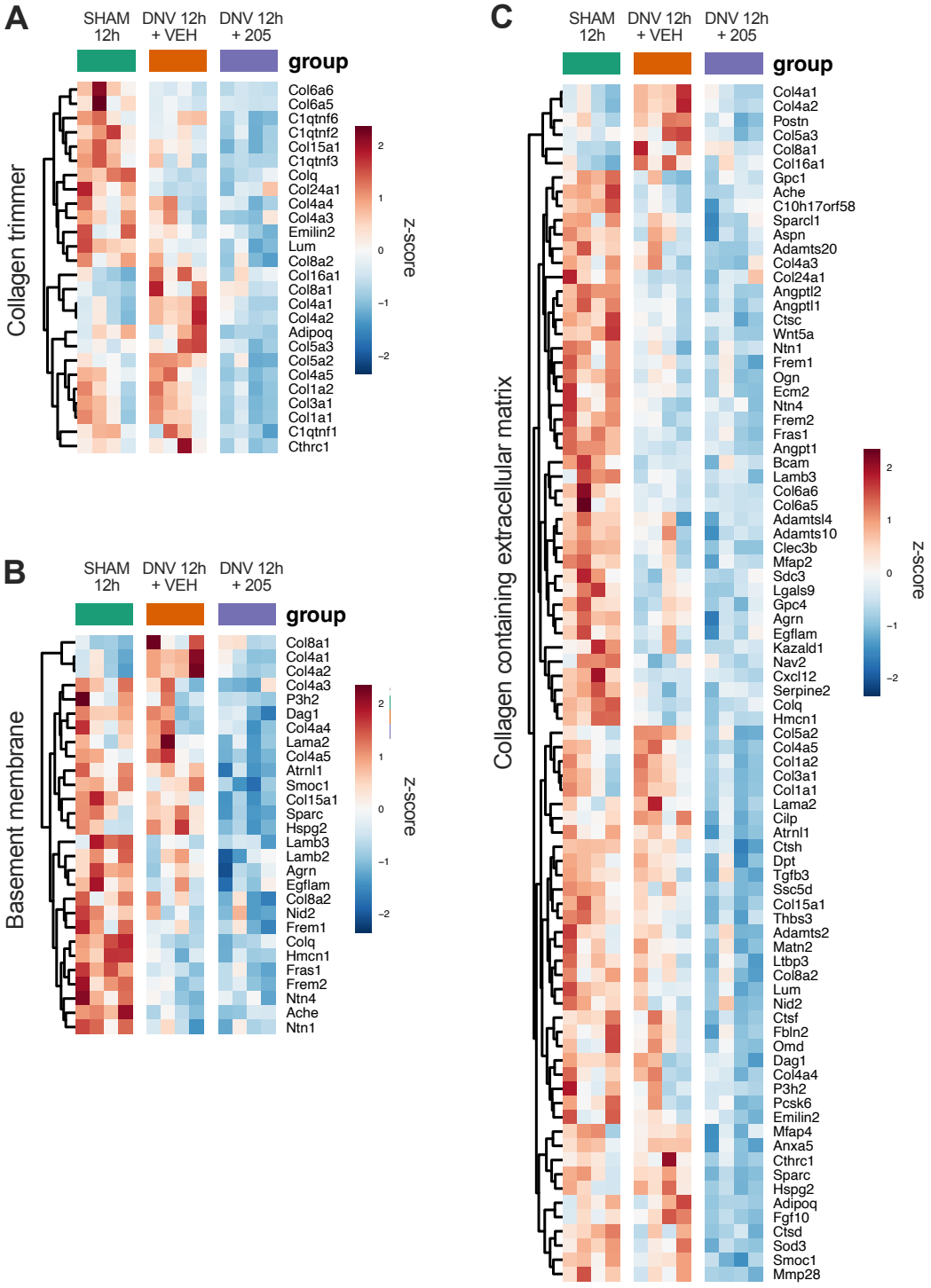
A
SHAM 12h
DNV 12h + VEH
DNV 12h + 205
group
Collagen trimmer
Col6a6
Col6a5
C1qtnf6
C1qtnf2
Col15a1
C1qtnf3
Colq
Col24a1
Col4a4
Col4a3
Emilin2
Lum
Col8a2
Col16a1
Col8a1
Col4a1
Col4a2
Adipoq
Col5a3
Col5a2
Col4a5
Col1a2
Col3a1
Col1a1
C1qtnf1
Cthrc1
z-score
2
1
0
−1
−2
B
SHAM 12h
DNV 12h + VEH
DNV 12h + 205
group
Basement membrane
Col8a1
Col4a1
Col4a2
Col4a3
P3h2
Dag1
Col4a4
Lama2
Col4a5
Atrnl1
Smoc1
Col15a1
Sparc
Hspg2
Lamb3
Lamb2
Agrn
Egflam
Col8a2
Nid2
Frem1
Colq
Hmcn1
Fras1
Frem2
Ntn4
Ache
Ntn1
z-score
2
1
0
−1
−2
C
SHAM 12h
DNV 12h + VEH
DNV 12h + 205
group
Collagen containing extracellular matrix
Col4a1
Col4a2
Postn
Col5a3
Col8a1
Col16a1
Gpc1
Ache
C10h17orf58
Sparcl1
Aspn
Adamts20
Col4a3
Col24a1
Angptl2
Angptl1
Ctsc
Wnt5a
Ntn1
Frem1
Ogn
Ecm2
Ntn4
Frem2
Fras1
Angpt1
Bcam
Lamb3
Col6a6
Col6a5
Adamtsl4
Adamts10
Clec3b
Mfap2
Sdc3
Lgals9
Gpc4
Agrn
Egflam
Kazald1
Nav2
Cxcl12
Serpine2
Colq
Hmcn1
Col5a2
Col4a5
Col1a2
Col3a1
Col1a1
Lama2
Cilp
Atrnl1
Ctsh
Dpt
Tgfb3
Ssc5d
Col15a1
Thbs3
Adamts2
Matn2
Ltbp3
Col8a2
Lum
Nid2
Ctsf
Fbln2
Omd
Dag1
Col4a4
P3h2
Pcsk6
Emilin2
Mfap4
Anxa5
Cthrc1
Sparc
Hspg2
Adipoq
Fgf10
Ctsd
Sod3
Smoc1
Mmp28
z-score
2
1
0
−1
−2

Table 1.

ENSEMBL ID	Gene Symbol	Gene Biotype	Chromosome	Base Mean	Log2 Fold Change	lfcSE	p-value	padj
UP								
ENSRNOG00000016437	Tm4sf4	protein_coding	2	17,6122429	3,789838599	1,203520958	1,75071E-06	0,001204378
ENSRNOG00000005964	Nr4a3	protein_coding	5	283,3148153	1,606680313	0,65174188	8,04E-06	0,004055837
ENSRNOG00000042717	Ciart	protein_coding	2	47,50701374	1,087136024	0,241878824	2,134E-07	0,000240969
ENSRNOG00000012410	S100a1	protein_coding	2	106,230202	0,806337451	0,179253103	6,33191E-07	0,000560089
ENSRNOG00000026519	Pkm-ps20	pseudogene	20	87,81533493	0,596757872	0,391477297	0,000224519	0,049981909
ENSRNOG00000011262	Bicra	protein_coding	1	352,0030887	0,566342079	0,18605263	1,60898E-05	0,00658292
ENSRNOG00000038212	Socs6	protein_coding	18	357,1032721	0,504293982	0,239060527	8,12826E-05	0,023662613
DOWN								
ENSRNOG00000008310	Mpo	protein_coding	10	30,68728358	-4,477626874	0,86497719	1,23056E-08	3,10471E-05
ENSRNOG00000021207	Lgals12	protein_coding	1	16,63787864	-4,226564414	1,462497668	1,63231E-06	0,001176662
ENSRNOG00000002834	Klb	protein_coding	14	15,17946604	-3,653141743	0,722901877	3,1499E-08	5,96041E-05
ENSRNOG00000012674	Adrb3	protein_coding	16	20,96107168	-3,344566786	0,622993833	7,83432E-09	2,37192E-05
ENSRNOG00000028616	Pck1	protein_coding	3	316,026661	-3,239192936	0,449947119	1,29121E-13	1,95463E-09
ENSRNOG00000046858	Arxes2	protein_coding	X	8,819805912	-3,068825083	1,295518258	6,734E-06	0,003533777
ENSRNOG00000046858	Arxes1	protein_coding	X	8,819805912	-3,068825083	1,295518258	6,734E-06	0,003533777
ENSRNOG00000015086	Plin1	protein_coding	1	284,6420376	-3,002527864	0,639015708	8,30602E-08	0,000125737
ENSRNOG00000049351	Nat8l	protein_coding	14	33,73179932	-2,809515359	0,684655737	3,75906E-07	0,000355654
ENSRNOG00000001821	Adipoq	protein_coding	11	607,3094283	-2,658603085	0,609454255	1,55575E-07	0,000196258
ENSRNOG00000009153	Cidec	protein_coding	4	319,8284686	-2,639766654	0,454193794	2,75621E-10	1,90248E-06
ENSRNOG00000011892	Slc36a2	protein_coding	10	23,77518803	-2,610864966	0,971462989	4,89381E-06	0,00284933
ENSRNOG00000001295	S100b	protein_coding	20	138,0192366	-2,598281841	0,52717817	1,73533E-08	3,75278E-05
ENSRNOG00000013097	C6h14orf180	protein_coding	6	16,4152481	-2,410504532	1,098357941	1,05224E-05	0,004704953
ENSRNOG00000005792	Ankef1	protein_coding	3	40,92764889	-2,287926971	0,871341313	5,35876E-06	0,00300448
ENSRNOG00000004828	Acvr1c	protein_coding	3	9,367554476	-2,259186154	1,653522054	3,58143E-05	0,012908502
ENSRNOG0000	Prkar2b	protein_c	6	186,361	-	0,60679	7,87982	0,00062

0009079		oding		0277	2,151611484	6375	E-07	7814
ENSRNOG00000003442	Adora1	protein_coding	13	68,96023553	-2,116664501	0,48780618	5,4613E-08	9,18591E-05
ENSRNOG00000001001	Retn	protein_coding	12	176,1481687	-2,097250535	0,583972591	6,6598E-07	0,000560089
ENSRNOG00000012278	Fgf10	protein_coding	2	7,061425597	-1,811214281	1,476219539	5,76646E-05	0,01857291
ENSRNOG00000015071	Zim1	protein_coding	1	72,74520752	-1,725675207	0,546423231	1,82988E-06	0,001204378
ENSRNOG00000033564	Cfd	protein_coding	7	341,3879947	-1,618698388	0,396036993	1,0744E-07	0,000147856
ENSRNOG00000008956	Cdkn2c	protein_coding	5	39,78068637	-1,571364197	0,400702292	2,22854E-07	0,000240969
ENSRNOG00000022946	Slc22a3	protein_coding	1	35,26224121	-1,546451726	0,647987749	9,70743E-06	0,00459222
ENSRNOG00000000158	Cdo1	protein_coding	18	475,4382482	-1,494996513	0,282306833	3,77026E-10	1,90248E-06
ENSRNOG00000011417	Pde3b	protein_coding	1	70,10126466	-1,275540592	0,599106026	2,08486E-05	0,008305415
ENSRNOG00000003357	Col3a1	protein_coding	9	12381,13309	-1,269296892	0,412765196	4,54009E-06	0,002830397
ENSRNOG00000022268	Pnpla3	protein_coding	7	66,42415379	-1,226076719	1,362324254	0,000145765	0,036173668
ENSRNOG00000018951	Col4a5	protein_coding	X	246,4573269	-1,172681715	0,271286522	2,56263E-07	0,000258621
ENSRNOG00000012840	Sparc	protein_coding	10	9459,030856	-1,145582612	0,219721436	5,42177E-09	2,05187E-05
ENSRNOG00000016681	Mc2r	protein_coding	18	6,745401153	-1,044223744	1,376734915	0,000215527	0,049433986
ENSRNOG00000068207	ENSRNOG00000068207	lncRNA	2	71,69491139	-1,040907016	0,337064148	8,52713E-06	0,004163992
ENSRNOG00000059894	Hmmr	protein_coding	10	14,3711061	-1,01971652	0,746399567	9,21002E-05	0,024896662
ENSRNOG00000019265	Pcdh12	protein_coding	18	97,81810717	-1,00564771	0,288661155	4,67432E-06	0,002830397
ENSRNOG00000029911	Cilp	protein_coding	8	350,9021455	-0,996386598	0,302124862	6,76969E-06	0,003533777
ENSRNOG00000003897	Col1a1	protein_coding	10	5473,455718	-0,972013538	0,595029291	7,39457E-05	0,022035732
ENSRNOG00000060381	Col15a1	protein_coding	5	1094,025407	-0,970012729	0,238654195	1,41264E-06	0,001069228
ENSRNOG00000005998	Smoc1	protein_coding	6	43,56168462	-0,961648386	0,625367727	8,46648E-05	0,024182175
ENSRNOG00000049614	Itih5	protein_coding	17	259,6072555	-0,954845167	0,321664858	1,3057E-05	0,005647348
ENSRNOG00000022239	Trarg1	protein_coding	10	215,502458	-0,946272472	0,508271459	6,02012E-05	0,018985952
ENSRNOG00000048924	Islr	protein_coding	8	96,75848625	-0,932560953	0,475548876	5,52929E-05	0,018196186

ENSRNOG00000014791	Peg3	protein_coding	1	1008,607567	-0,929639141	0,296025766	1,05673E-05	0,004704953
ENSRNOG00000029465	Slc26a10	protein_coding	7	318,7370695	-0,92657907	0,520335672	6,97254E-05	0,021540881
ENSRNOG00000012660	Postn	protein_coding	2	407,3694786	-0,926272454	0,581975445	8,67208E-05	0,024310733
ENSRNOG00000017406	Atrnl1	protein_coding	1	86,66961975	-0,922922419	0,351946922	2,36397E-05	0,009175822
ENSRNOG00000007059	Atp1b4	protein_coding	X	126,8800026	-0,903643521	0,647470525	0,000113779	0,030217437
ENSRNOG00000020525	Col5a3	protein_coding	8	282,2641751	-0,849485674	0,381327901	4,85208E-05	0,01632241
ENSRNOG00000003869	Sod3	protein_coding	14	344,0210729	-0,841802222	0,322322641	2,88874E-05	0,010665786
ENSRNOG00000026114	Ap5b1	protein_coding	1	71,33655764	-0,825421112	0,301195018	2,46814E-05	0,009340692
ENSRNOG00000011921	Dusp4	protein_coding	16	58,03429501	-0,820283796	0,576863771	0,000137595	0,0359122
ENSRNOG00000020546	Lipe	protein_coding	1	652,1235112	-0,778821842	0,383241395	7,42385E-05	0,022035732
ENSRNOG00000047940	Mmp28	protein_coding	10	28,56867425	-0,761946897	0,618130313	0,000194535	0,045651031
ENSRNOG00000018865	Adamts12	protein_coding	2	166,9839783	-0,71216855	0,432342073	0,000144709	0,036173668
ENSRNOG00000007370	Rnf144a	protein_coding	6	34,97523865	-0,680235649	0,414843868	0,000158104	0,038602792
ENSRNOG00000003736	Col5a2	protein_coding	9	961,2698157	-0,677069523	0,265562027	4,01151E-05	0,014122369
ENSRNOG00000007300	C1qtnf6	protein_coding	7	61,36282397	-0,674758918	0,492847777	0,000223652	0,049981909
ENSRNOG00000005323	Syne2	protein_coding	6	714,2872969	-0,592748527	0,234918406	4,19457E-05	0,014431222
ENSRNOG00000021437	Hspg2	protein_coding	5	3301,965162	-0,586663851	0,187505171	1,43459E-05	0,006032463
ENSRNOG00000043192	Hacd1	protein_coding	17	302,3667613	-0,574867934	0,337959209	0,00017446	0,041920198
ENSRNOG00000016281	Col4a1	protein_coding	16	4047,849222	-0,560805627	0,34135596	0,000196018	0,045651031
ENSRNOG00000023400	Dtx3l	protein_coding	11	119,2932824	-0,555706162	0,303233193	0,000140476	0,03604287
ENSRNOG00000021237	Dnaaf9	protein_coding	3	161,2939517	-0,521175226	0,25306968	9,13532E-05	0,024896662